Large impacts and their contribution to the water budget of the Early Moon

T. Engels, Julien Monteux, Maud Boyet, Mohamed Ali Bouhifd

Large impacts and their contribution to the water budget of the Early Moon

T. Engels*[a], J. Monteux[a], M. Boyet[a], M.A. Bouhifd[a]

[a]*Laboratoire Magmas et Volcans, Université Clermont Auvergne, CNRS, IRD, OPGC, F-63000 Clermont-Ferrand, France.*
Corresponding author: tristan.engels@uca.fr

Abstract

The Earth/Moon system likely results from a giant impact between a Mars-size object and the proto-Earth. This high-energy impact leads to extreme conditions under which volatile elements would not normally be preserved in the protolunar disk. However, recent measurements of lunar samples highlight the presence of a non-negligible amount of water in the Moon's interior (from 1.2 to 74 ppm). The aim of the present work is to quantify the water contribution of the late accretion on the early Moon. Here, we use a 2D axisymmetric model with the hydrocode iSALE-Dellen to study the fate of a large impactor on a target body similar to the early Moon with a crust, a magma ocean, and a mantle. For this purpose, we compute different models to monitor the depth to which the impacted material is buried at the end of the impact event and the degree of devolatilisation of the impactor. Three parameters are explored: the crustal thickness (ranging from 10 to 80 km), the impactor radius (ranging from 25 to 200 km) and the impactor velocity (ranging from 1 to 4 times the target escape velocity). Our models show that impactors with a radius greater than 25 km impacting a partially molten lunar body with a crust thinner than 40 km could significantly contribute to the water content of the lunar mantle even for impact velocities close to the lunar escape velocity. For impact velocities greater than 3 times the target escape velocity, the impactor material is significantly molten

and its water content is devolatilised within the lunar atmosphere. Depending on the water content of the impactor material and the ability of the lunar magma ocean to maintain chemical heterogeneities, the late lunar accretion following the Moon-forming giant impact could explain the differences in water content among the lunar samples.

Keywords: early moon, impact cratering, numerical modeling, LMO, late accretion

---

1. Introduction

Several tens of millions of years after the beginning of its accretion, the proto-Earth experienced a giant impact that led to the formation of the Earth-Moon system (*Hartmann and Davis*, 1975; *Woo et al.*, 2022). This collision with a proto-planet named Theia, whose radius was between 2000 and 4000 km, occurred when the core/mantle separation of the early Earth was almost fully achieved (*Cameron and Ward*, 1976; *Canup*, 2004; *Ćuk and Stewart*, 2012). Such a catastrophic event would have generated a large disk of molten debris or a synestia (*Lock et al.*, 2018) that re-accreted to form the Moon. Hence, after its accretion, the early Moon was probably significantly to fully molten (*Smith et al.*, 1970). A thick magma ocean made of molten silicate material (*Warren*, 1985) surrounded a relatively small metallic core compared to other terrestrial planets (*Wieczorek*, 2009). After rapid cooling of its surface, solidification occurred (1) from the bottom of the lunar magma ocean (LMO) forming a thick layer of olivine followed by the solidification of pyroxene material (*Charlier et al.*, 2018) and (2) at the surface of the Moon where a thin unstable crust formed in contact with the colder atmosphere (*Monteux et al.*, 2016a). Towards the end of the magma ocean stage, at 75-80% crystallisation (*Snyder et al.*, 1992; *Elkins-Tanton et al.*, 2011), a thick anorthositic crust had formed on the surface of the Moon (*Wood et al.*, 1970). It left a molten reservoir between the crust and the solidified deep lunar mantle (<1000 km-thick). The early Moon solidified over a timescale ranging from 10 Myrs (*Elkins-Tanton et al.*, 2011) to ≈200 Myrs after its formation (*Warren*, 1985; *Maurice et al.*, 2020; *Michaut and Neufeld*, 2022).

After the giant impact, the accretion of material continues and large to giant impacts occurred with consequences still visible from lunar observations

(e.g. *Zhu et al.* (2019a)). Thirty-two impact basins formed before 3.8 Gyr by impactors with diameters of more than 50 km are currently preserved on the surface of the Moon (*Garrick-Bethell and Zuber*, 2009; *Kamata et al.*, 2015; *Morbidelli et al.*, 2018). The South Pole-Aitken (SPA) basin (with a diameter of about 2500 km) is the largest preserved impact basin and one of the oldest preserved structures observed on the Moon (*Garrick-Bethell and Zuber*, 2009; *Evans et al.*, 2018; *James et al.*, 2019). This crater could be the consequence of a large impact with an impactor of ≈160 km in diameter (*Potter et al.*, 2012; *Trowbridge et al.*, 2020; *Miljković et al.*, 2021). However larger impact events likely occurred throughout the lunar accretion and the Procellarum basin might be a remnant of such a giant impact (*Nakamura et al.*, 2012). The origin of the Procellarum basin, which is even larger (with a diameter of about 3200 km) and older is still under debate (*Andrews-Hanna et al.*, 2014; *Zhu et al.*, 2019b) . *Zhu et al.* (2019a) estimated that more than 200 basin-forming impacts (with crater diameter > 300 km) occurred between the giant impact event and the end of crystallisation of the magma ocean. Large impacts likely contributed to the final chemical and thermal evolution of the Moon (*Bottke et al.*, 2010). These large impacts are expected to have occurred in a context where the Moon was still significantly molten (see e.g. *Miljković et al.* (2021)), favouring chemical exchanges between the impactor material and the magma ocean beneath the solid crust.

The water content within the lunar interior has been estimated from H measurements carried out on volatile-bearing phases (see references in *McCubbin et al.* (2023): lunar apatites, glass beads and mesostasis glasses, melt inclusions, and nominally anhydrous minerals. It is non-trivial to determine the lunar water content in the lunar interior from these measurements because several processes

such as spallation or degassing may have modified this content and/or might be representative of an evolved magmatic source that is chemically different from the bulk lunar mantle. Chemical analyses of the lunar rocks sampled from the Apollo mission initially indicated that the lunar rocks were depleted in moderately volatile elements (*Lunar Sample Preliminary Examination Team*, 1969). Moderately volatile elements are elements with condensation temperatures between those of Mg-silicates and FeS (*Palme et al.*, 1988). *Borg et al.* (2022) highlighted that the absence of these moderately volatile elements could have been caused by the formation of the two bodies involved in the creation of the Earth-Moon system. Moreover, the Moon formation scenario favours extreme conditions (with a temperature increase of at least ∼5000 K) and, as a consequence, a depletion in volatile elements in the Moon's interior (*Canup*, 2008). Due to high impact temperatures and outgassing of the LMO, the Moon's interior should have experienced an important depletion in volatile elements during its accretion (*Boyce et al.*, 2015). However, more recent chemical analyses of lunar samples have shown a variable water content from 1.2 to 74 ppm within the lunar mantle (*Saal et al.*, 2008; *Tartèse et al.*, 2013; *Füri et al.*, 2014; *Nakajima and Stevenson*, 2018; *Stephant et al.*, 2020; *Hu et al.*, 2021). The wide range in water content within lunar samples seems to represent a degree of heterogeneity within the lunar mantle in terms of water content (*Robinson and Taylor*, 2014; *Robinson et al.*, 2016; *McCubbin et al.*, 2023).

The solidification processes that occurred within the Moon, combined with the occurrence of large impacts while molten reservoirs were still present (*Perera et al.*, 2018; *Zhu et al.*, 2019a) may have favored the incorporation of hydrated objects deep within the lunar mantle. Large impacts likely contributed to the water budget of the Moon (*Bottke et al.*, 2010) and induced significant produc-

tion of ejectas, melt and vapor (*Pierazzo et al.*, 1997; *Luo et al.*, 2022). The contribution of the impactors to the lunar volatile content is strongly dependent on the impact velocity (*Svetsov and Shuvalov*, 2015). Tracking impactor material within impacted bodies is now possible with the improvement of numerical modeling. *Potter and Collins* (2013) focused on the likelihood of the impactor remaining solid as a function of its characteristics (porosity, shape, impact velocity and angle) and proposed possible scenarios in which this material would remain within the crater. Then, *Svetsov and Shuvalov* (2015) focused on low-velocity impacts to determine the water content and the mass fraction remaining at the bottom of the craters with the Eulerian method in the iSALE hydrocode. More recently, *Kendall and Melosh* (2016) investigated the iron core stretching of a large impactor in a terrestrial magma ocean using tracers with the iSALE-3D hydrocode model. Finally, *Marchi et al.* (2018) used a hydrocode with the SPH method to track the iron core of a large impactor with a more realistic 45° angle.

In the present study, we monitor the fate of an impactor and its associated depth distribution in a magma ocean beneath a solid crust. Our aim is to constrain the water contribution of large impacts at the time when the deep Moon was still significantly molten. For that we use the hydrocode iSALE to investigate the ability of an impactor to penetrate deep into the interior of the Moon as a function of three parameters: the lunar crustal thickness, the impactor radius and the impact velocity. Our manuscript is organised as follows: In section 2 we describe our physical and numerical models. We illustrate our modelling approach with a reference model in the section 3. In the section 4 we monitor the fate of the impactor using a parametric study. The section 5 discusses the evolution of the pressure and temperature of the impacted material as a func-

tion of the three parameters described above. In the section 6 we discuss the ability of large impacts to contribute to the water budget of the LMO and the limits of our model.

2. Impact modelling: Methods

During the first few Myrs after the giant impact that led to the Moon's formation, more than 200 impact basins (with diameters of more than 300 km) were likely formed (*Zhu et al.*, 2019a). These impacts occurred while molten reservoirs were likely still present within the deep Moon. In our study, we performed numerical hydrocode simulations to model a large impact event on a Moon-sized body with a magma ocean. For that, we used iSALE-2D shock physics code (*Wünnemann et al.*, 2006), which is based on the SALE hydrocode solution algorithm (*Amsden et al.*, 1980; *Melosh et al.*, 1992; *Ivanov et al.*, 1997). The code iSALE-2D is a multi-rheology, multi-material model that enables to model large impacts on a planetary scale (*Monteux et al.*, 2014; *Bray et al.*, 2014; *Monteux and Arkani-Hamed*, 2019; *Trowbridge et al.*, 2020). iSALE simultaneously solves the equations of conservation of mass, energy and momentum with constitutive relations for material properties. We used the most recent version which is iSALE-Dellen (*Collins et al.*, 2016).

During a large impact on a rocky body, three stages occur: contact and compression stage, excavation stage and the modification stage (*Melosh*, 1989; *Collins et al.*, 2012). The excavation phase leads to the opening of a crater while the modification stage alters its structure over a longer timescale to its final state. The presence of a molten layer within the interior of the impacted target may influence the deformation processes during the impact. *Monteux*

et al. (2016b) showed that the presence of a thick water ocean within Enceladus was reducing the impact-induced deflection of the solid core surface beneath the ocean. More recently, *Miljković et al.* (2021) showed the influence of a thin melt layer on the basin-forming process, where magma flow dominates the crater collapse and changes its final morphology. In the following sections, we describe our modelling approach to a large impact on a partially molten Moon.

2.1. Characteristics of the impact

After the Moon forming impact, large impacts continued to deliver material to the Moon. The distribution of impact velocities on the Moon is similar to that for the Earth, although they are shifted to lower values because the Moon has a lower gravity. If coming from the asteroid orbit, the impact velocity distribution has a maximum at about 12 km s^{-1} (*Bottke et al.*, 2002). This peak in velocity distribution is a function of the impactor size and ranges from 10 to 15 km s^{-1} (*Marchi et al.*, 2009). A non negligible fraction of the lunar crater occurred with a velocity lower than 10 km s^{-1} (*Ito and Malhotra*, 2010; *Le Feuvre and Wieczorek*, 2011), the lower bound of the impact velocity being the lunar escape velocity (= 2.38 km s^{-1}). In our models we use impact velocities v_{imp} ranging between 1 and 4 times the escape velocity v_e of our modelled planet (corresponding to 2.33 and 9.32 km s^{-1} respectively). The upper bound of impact velocity is chosen to limit numerical instabilities and corresponds to the typical velocity on the Moon (*Marchi et al.*, 2012).

Impact angles (θ) potentially range between 0° and 90° with respect to the tangent of the impacted planet's surface (90° being a vertical impact). Accretionary models that have taken into account moderately oblique impacts do not show a significant influence of impact angle on the final state of an accreted body

(*Agnor and Asphaug*, 2004; *Kokubo and Genda*, 2010). However, decreasing the impact angle from 90° to 45° (the most probable impact angle (*Shoemaker*, 1962)) leads to a reduction in shock pressure by a factor of ~ 0.71 (see *Pierazzo and Melosh* (2000a)). For extremely low impact angles (with $\theta \leq 30°$), the impactor will not penetrate into the target (e.g. *Elbeshausen et al.* (2009)). In our models and as first step, we consider only head-on collisions (impact angle of 90° to the target tangent plane). The role of impact angle is left to future studies. Hence, we used 2D cylindrical geometry models, less costly in computation time than a 3D model.

2.2. Characteristics of the impactor

The ability of an impactor to contribute to the water content of the impacted Moon is governed by its composition and its origin. The water could have been delivered to the Moon by comets and/or asteroids (*Bruck Syal and Schultz*, 2015; *Barnes et al.*, 2016). According to *Nesvorný et al.* (2023), the contribution of the comets is not significant during the early bombardment of the Moon. Recent studies have shown that the early impactors of terrestrial planets are likely to be leftover planetesimals formed in the terrestrial planet region (*Morbidelli et al.*, 2018; *Zhu et al.*, 2021; *Nesvorný et al.*, 2023). In this scenario, the impactors would likely be differentiated and the water contribution of the late accretion could be relatively poor. If we consider aubrites, that are achondrites produced by igneous differentiation of the enstatite chondrite, they have water contents three orders less than those of ECs (*Lorenz et al.*, 2021). Other studies, however, argue that hydrogen was delivered to the Earth/moon system by accretion of chondritic material (*Tartèse and Anand*, 2013; *Saal et al.*, 2013; *Füri et al.*, 2014). More recent models show that the accretion of terrestrial planets is a heterogeneous process, whereby predominant accretion of volatile-poor planetesimals was followed by a second volatile-rich stage from undifferentiated

meteorites (*Liu et al.*, 2023). As a consequence and for simplicity, we assume that the potential water contribution from the impactors range between water-poor (enstatite chondrites) to volatile-rich (CI chondrites). However, depending on the type of chondrite envisioned, large differences in the water content may arise among the impactors. Nearly 500 planetesimals with a radius larger than 10 km have impacted the Moon since its formation (*Nesvorný et al.*, 2023). The presence of large impact craters such as SPA or Procellarum suggest that the range of impactor radii may exceed 100 km in diameters (e.g. *Melosh et al.* (2017); *Zhang et al.* (2022); *Jones et al.* (2022)). In our study, we consider that the impactor radius (R_{imp}) ranges between 25 and 200 km.

Depending on its evolution, a large metallic core is also likely to be present within the impactor. However, unless they formed rapidly, even large impactors might have been too small to have experienced metal/silicate separation (*Ricard et al.*, 2017). If the impactors are leftover planetesimals formed at the early Solar System as suggested by *Zhu et al.* (2021) or *Nesvorný et al.* (2023), the impactors with a diameter larger than 10 km could be differentiated. For simplicity, and as a first step towards more complex models, the impactor is assumed to be a spherical body with a uniform solid composition. The presence of a metallic core within the impactor would increase its mass and as a consequence its kinetic energy. Hence, considering a homogeneous impactor in our models is a conservative assumption.

2.3. Characteristics of the target

According to the giant impact scenario, the Moon's mantle is thought to be derived from the silicate Earth's mantle (*Canup*, 2012; *Ćuk and Stewart*, 2012; *Hosono et al.*, 2019). After its re-accretion, the lunar mantle remained signif-

icantly molten with an estimated magma ocean depth of 400 km to 1200 km (*Snyder et al.*, 1992; *Charlier et al.*, 2018; *Shearer*, 2006). During the solidification of a potentially fully molten lunar mantle, the first mineral to crystallise would have been olivine. The crystallisation of the olivine likely began from the bottom of the magma ocean and formed a 300-500 km-thick solid layer. Upon cooling, orthopyroxene and then clinopyroxene phases would have solidified (*Solomatov*, 2007; *Elkins-Tanton et al.*, 2011; *Charlier et al.*, 2018; *Johnson et al.*, 2021; *Kraettli et al.*, 2022). When the magma ocean was ≈75-80% solidified, fractional crystallisation of the residual melt resulted in the formation of the anorthositic lunar crust by floatation of the plagioclase crystals (*Snyder et al.*, 1992; *Elkins-Tanton et al.*, 2011). During this last crystallization phase, a thin crust formed over the remaining molten material. In the classical models of magma ocean fractional crystallization, the thickness of the magma ocean when the anorthite lunar crust starts to form ranges between 110 and 200 km (*Maurice et al.*, 2020). Assuming that the convection is vigorous enough to maintain a slushy material with a cristal fraction of up to 50%, the thickness of the slush (that should behave as a liquid) may encompass the full thickness of the lunar mantle when the crust starts to form (*Michaut and Neufeld*, 2022). In our study, we consider impacts occurring early during the lunar magma ocean cooling and arbitrary fix the bottom of the magma ocean to 300 km. Hence the magma layer in our models is much thicker compared to 10-50 km as used in *Miljković et al.* (2021).

Hence, for 150 to 200 million years after the Moon forming impact, a magma ocean was encompassed between a thick solid mantle and a crust with a thickness increasing through the lunar cooling process (*Maurice et al.*, 2020). Currently, the entire silicate material of the Moon is supposed to be solid and its crust

is on average between 34 and 43 km thick with maximum value up to 60 km (*Wieczorek et al.*, 2013). In our study, we modelled the collision between an impactor made of silicate material and a Moon-size target (with radius $R = 1740$ km) composed of three homogeneous layers:

1. a solid dunitic mantle with a constant thickness 1440 km-thick,
2. an intermediate dunitic magma ocean with a thickness (220 to 290 km) that depends on the chosen thickness for the lunar crust,
3. a thin solid crust. To identify the influence of the crustal thickness on the penetration ability, we consider a range of crustal thickness values with an upper bound value larger than the lunar crustal thickness. We consider a crustal thickness ranging between 10 and 80 km.

In our models, we do not consider the Moon's core is to be affected by the impacts. The core size of the Moon is expected to be small compared to its mantle thickness (with a radius ≈ 380 km according to *Garcia et al.* (2011)). In our models, we do not include the presence of a dense metallic iron core within the impacted Moon. This results in a surface gravity and, as a consequence, an escape velocity that are slightly lower on our modelled lunar target ($= 2.33$ km s^{-1}) than on the Moon ($= 2.38$ km s^{-1}). This difference in surface gravity is small enough to not affect neither the cratering formation processes nor our results and interpretations.

2.4. Properties of the involved material

The thermodynamic parameters (pressure, volume, temperature, internal energy) of the materials from our models are characterised by equations of state (EOS) for each material (crust, magma ocean, mantle and impactor). To characterise the material behaviour during the impact, we use two chemical rock

compositions with their corresponding EOS: granite for the crustal material and dunite for the impactor, the magma ocean and the mantle. The thermo-dynamic properties and equations of state for chondritic material are not available in the materials proposed by iSALE. Hence we use dunitic material for the impactor material (*Pierazzo and Melosh*, 2000b; *Zhu et al.*, 2019a). We used the semi-analytical EOS (ANEOS) to model the thermodynamic behaviour of the dunitic material (*Benz et al.*, 1989; *Thompson*, 1990) (see Tab. 1). The Moon's crust is anorthositic and was formed by plagioclase floatation (*Smith et al.*, 1970; *Wood et al.*, 1970). However, in iSALE Dellen no such material is available. Hence, we used the ANEOS model of granitic material whose density is similar to the density of the anorthosite. This choice is relevant for modeling the thermodynamic response of the anorthositic crustal material during a large impact event (*Melosh et al.*, 2013; *Johnson et al.*, 2018; *Trowbridge et al.*, 2020; *Miljković et al.*, 2021).

During an impact, the deformation of intact rock occurs in different steps. When a constant pressure is applied to the rock, it first deforms elastically, proportionally to the stress without accumulating damage up to a certain threshold. Then it deforms plastically and the rock damage is accumulated permanently until fracturing occurs. At this point, the damage is maximal, the rock becomes fully fractured and the strength is controlled by rock friction (*Collins et al.*, 2004). In this context, the material strength strongly influences the crater morphology as well as the post-shock temperature increase within the impact site. Hence considering a relevant strength model is crucial for modelling the deformation of both the impactor and the target and their temperature evolutions (*Wakita et al.*, 2019, 2022). iSALE includes numerous strength models for solid and granular material, ranging from simple (Lundborg) to complex (Johnson-Cook). For solid material (crust, impactor and mantle) we used the

ROCK model, which is a combination of Lundborg's equations with a damage parameter computed by the damage model (see Tab. 1). With this model, the deformation is sensitive to the state of the material which becomes weaker as the damage increases. For liquid behaviour, there are two models in iSALE: a Newtonian fluid model (with viscosity) and an inviscid fluid model (without viscosity). The magma ocean is a thick layer of molten rock with low viscosity in which there is vigorous convection (*Solomatov*, 2007). In such a reservoir, the magma viscosity may range between 10^{-1} and 10^{2} Pa s (*Solomatov*, 2007). Our simulations assume a fully molten inviscid magma ocean to reproduce purely hydrodynamic behaviour (*Kendall and Melosh*, 2016).

The strength model influences how the kinetic energy from the impactor is converted into heat within both the impactor and the impacted material. During an impact, the shock compression is the main contributor to the impact induced heating. However, for low-velocity impacts (with $v_{imp} \leq 10$ km s^{-1}) both the compression and decompression have to be accounted for the calculation of the impact-induced temperature increase (*Pierazzo et al.*, 1997; *Zhu et al.*, 2017; *Kurosawa and Genda*, 2018; *Manske et al.*, 2021). *Kurosawa et al.* (2021) also illustrated that plastic deformation during low-speed collisions (with $v_{imp} \leq 10$ km s^{-1}) efficiently converts kinetic energy into internal energy within the shocked rocks. As a result, the degree of impact heating during low-speed collisions should be higher than if only the shock compression was considered. As a consequence, plastic work and decompression by structural uplift also contribute to melt production (*Manske et al.*, 2022). A common approach to quantify impact induced melt production is to monitor the amount of material that experiences shock pressures larger than the critical shock pressure for melting (e.g. *Pierazzo et al.* (1997)). In our study, we estimate the temperature in-

crease by monitoring directly the temperature from the iSALE models from the beginning of the contact up to nearly 4000 s after the impact. This method is similar to the final temperature method and is relevant for low-velocity impacts (*Quintana et al.*, 2015; *Manske et al.*, 2022). We then compare the obtained temperature with the melting temperature of chondritic material for a given pressure to estimate the melt fraction. This method may suffer from artificial diffusion (*Artemieva*, 2007). However, *Manske et al.* (2022) have shown that, in the early stage of the simulations, this direct temperature method provides accurate results of the total melt production.

A damage model is used to describe how the strength transition between an intact and a fractured material occurs. Three damage models are available in the iSALE code. The simple model takes a damage parameter that is a linear function of the plastic strain. In the *Ivanov et al.* (1997) model, damage is also a function of plastic strain. However, the plastic strain when rupture is reached is an increasing function of the total pressure P (lithostatic pressure plus the pressure induced by the shock). This model allows for rapid brittle failure under tension at low pressure and semi-brittle failure at high pressure. In the damage model developed by *Collins et al.* (2004), the plastic deformation at failure is a function of the brittle-ductile and brittle-plastic transition pressures. Our study focuses on impact processes occurring at relatively low impact velocities and inducing relatively low impact pressures. In this context, the Hugoniot Elastic Limit (HEL) is not necessarily overcome and both the impacted material and the impactor can fail in tension (*Wiggins et al.*, 2019). To characterize the influence of the failure in tension at very low impact velocity, we have compared models including a Ivanov damage model with models explicitly accounting for tensile failure: the Collins damage model. In the Collins model, the tensile strength

is explicitly stated as $Y_t = Y_{t0}(1 - D)$ with Y_{t0} the intact tensile strength and D the damage. Our results (not shown here) indicate that considering a Collins damage model neglecting tensile failure enhances the penetration of the impactor that penetrates 13% deeper than the Ivanov damage model at the end of the simulation. Including the tensile failure (with a tensile strength parameter of 10 MPa (*Trowbridge et al.*, 2020)) in the Collins model decreases this depth difference from 13% to 8%. Hence, neglecting tensile failure leads to a slightly overestimation of the penetration of the projectile. For the lowest impact velocities, the difference in the penetration depth between the Ivanov damage model and the Collins damage model including tensile failure is only 4%. Our conclusion is that including the tensile strength increases the resistance of the impacted material and decreases the depth reached by the impactor's material. However, the influence of the tensile failure appears to be less important than the choice of the damage model itself on the penetration ability of the impactor. Since the parameters in the Collins damage model are poorly constrained in the context of primitive protoplanets, we choose to use the Ivanov model as our damage model (*Ivanov et al.*, 1997).

Ostrowski and Bryson (2019) reported the average porosity for different types of chondritic material in the Solar System. The enstatite chondrites have the lowest porosity (between 2.1 and 3.7%) while the CI chondrites are composed mainly of hydrated phyllosilicate matrix and have a porosity of nearly 35%. Porosity may play a important role in the efficiency of impact heating (*Davison et al.*, 2010) and on the dehydration processes (*Sekine et al.*, 2015). iSALE allows to include the influence of porosity on impacts models (*Wünnemann et al.*, 2006). However, only three materials are allowed when modelling large impacts using iSALE with *Planet mode*. In our models, we

already consider three materials: the crust, the magma ocean and the mantle. To avoid a fourth material, both the impactor and the mantle are made of the same material (dunite). We note here that using dunitic material (with a low porosity) as a proxy for CI chondritic material (with a high porosity) is a strong assumption since the dunite should be significantly denser than CI chondrites. Adding porosity to this dunitic material means lowering the densities of the impactor and the impacted mantle. Hence, the impacted mantle would become less dense than the overlying magma ocean resulting in gravitational instabilities and potential large scale overturns. *Davison et al.* (2010) showed that for high velocity impacts between planetesimals, the impact heating was increasing with porosity. However, according to their models, this effect is relatively small for porosities lower than 30% and for the range of impact velocities envisioned in our study. Therefore, we do not include the effect of porosity in our models.

We used a pre-impact temperature profile that is conductive in the crust and convective in magma ocean (Figure 1). The choice of gradient influences the depth at which the neutral buoyancy of the impactor material will be reached within the magma ocean. For each crustal thickness considered in our study, the temperature gradient meets the solidus of the dunitic material at the bottom of the magma ocean.

Large impact simulations are likely to favor weakening processes (e.g. low density weakening or acoustic fluidization) facilitating deep-seated uplift of the crater floor and collapse of the rim (*Collins*, 2014). These processes result in complex craters formation. Material weakening by thermal softening is especially efficient for large-scale events (*Potter et al.*, 2012). This process strongly depends on the pre-shocked temperature profile that is still poorly constrained

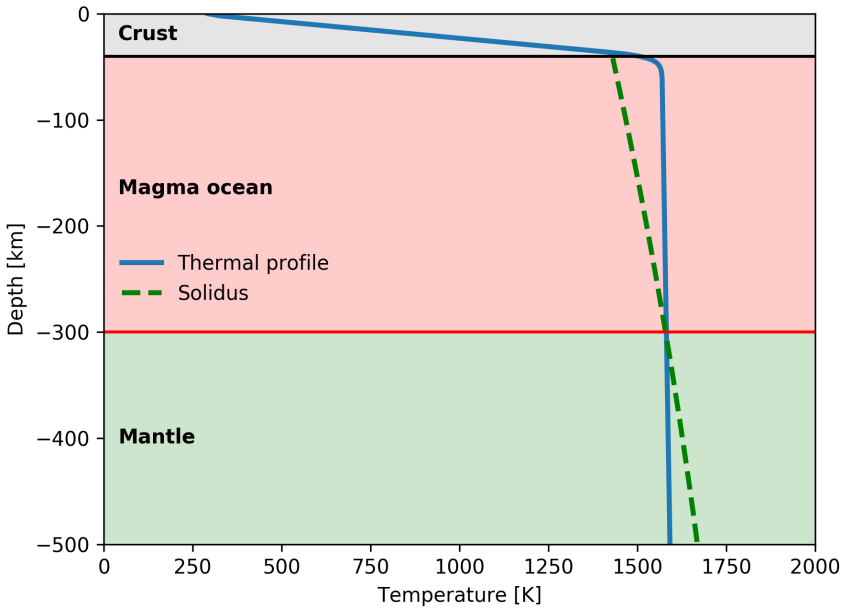

Figure 1: Initial temperature profile (blue curve) for the reference model considering a 40 km thick crust. The green curve represents the dunitic solidus from *Andrault et al.* (2018).

during the early evolution of terrestrial planets. Exploring the influence of this process would necessit the exploration of a wide range of pre-impact temperature profiles that is beyond the scope of this study. In the context of a liquid layer encompassed between two solid layers, this process might be of weak importance (*Monteux et al.*, 2016b). In our models, the acoustic fluidization is likely to play minor role on the shockwave propagation compared to that of the strength. For simplicity and to reduce the number of free parameters, we chose to neglect the low density weakening, the thermal softening and the acoustic fluidization. The influence of the processes (that can be accounted with iSALE models) favoring weakening and potentially affecting the impactor penetration will be explored in a separated study.

3. Reference model

For a better illustration of the different processes occurring during a large impact, we first consider a reference model from which we highlight the main stages of the temperature and pressure evolutions. In this reference model, we consider a 40 km thick crust, an impactor radius of $R_{imp} = 50$ km and an impact velocity $v_{imp} = v_e = 2.33$ km s^{-1}.

3.1. Description

Figure 2 shows the time evolution of the compositional (left) and temperature (right) fields during a large impact for this reference case (see Table 2). The temperature field is saturated to illustrate the impact-induced temperature increase in the impactor during each stage. Figure 2 (Top cross-section) shows the initial configuration of the two bodies before the impact. The cross-section obtained at $t = 315$ s shows the excavation stage leading to the formation of the transient crater on the Moon. In our study, we consider that the excavation stage ends when the transient crater reaches its maximum volume. The temperature increase ranges between 700 and 1700 K for the part of the impactor that is directly in contact with the Moon. The cross-section obtained at $t = 1200$ s illustrates the modification stage where the crater walls horizontally collapse followed by a vertical magma jet rising from the center of the crater. Vertical jets naturally form along the axis of symmetry and can be artifacts of the model setup. The heights of the jet obtained from our models do not show any exaggeration of this process (see Data availability Section). Similar processes are obtained from experimental analog models (*Landeau et al.*, 2021). The corresponding inflow generates a supplementary pressure increase. During this process, 0.81% of tracers reach a pressure increase of more than 5 GPa. This pressure increase is smaller than that generated during the contact/compression

stage where 47% of tracers demonstrate a pressure increase of more than 5 GPa (see also Section 5). During the modification stage, the average subsequent supplementary temperature increase is $\approx$ 120 K in the impactor material. Our reference model is a low velocity impact, hence the peak temperature and pressure increases are moderate. Depending on the impact parameters, it is possible for the impactor material to penetrate the crust and reach the magma ocean. In this reference case, the end of the simulation is fixed at $t = 4170$ s. At this time the impactor material has reached its final depth. A large crustal hole whose dimensions depend on the crustal thickness, impactor radius and impact velocity may remain at the lunar surface.

During the impact process, the impact energy dissipates within the impacted body as a function of time. As a consequence the subsequent deformation and movement of both the impactor and the impacted body decrease until an equilibrium is reached. To prevent the development of undesirable effects that are unrelated to the impact (e.g. numerical diffusion) and to save computation time, we included a simulation stop criterion based on the ratio between the average mass-weighted velocity of the impactor material obtained from the Eulerian method and the initial impact velocity. We stopped our simulations when this ratio fell below an arbitrary threshold value which we chose to fix at 1%. Figure 3 shows the ratio of the average of the velocity weighted to the mass of the impactor material over the initial impact velocity as a function of time for the reference model. This figure shows that the velocity of the impactor material decreases as a function of time during the early impact processes before oscillating during the late impact stages. These oscillations are due to the isostatic adjustment of the impactor in the magma ocean. In this reference model, we stopped our calculation $t = 4170$ s after the beginning of the impact. At

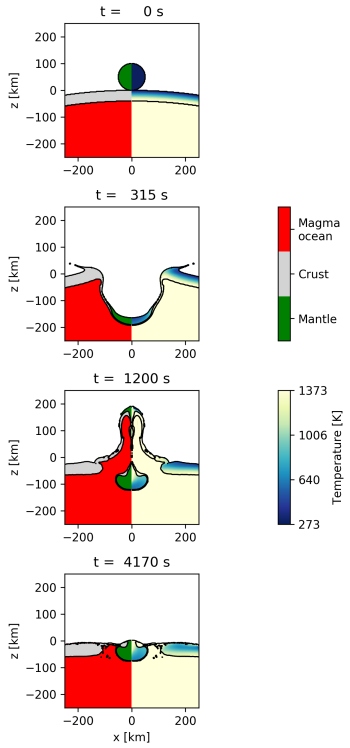

Figure 2: Evolution of the composition (left) and temperature (right) as a function of time. In our reference case ($v_{imp} = v_e = 2.33$ km s^{-1} and $\delta_{crust} = 40$ km), the undifferentiated dunitic impactor (green) ($R_{imp} = 50$ km) impacts a body with a 1740 km radius.The planet is composed of a shallow crust (gray), a magma ocean (red) and a mantle (green). The cross-section for $t = 0$ s represents the conditions before the impact. The cross-section for $t = 315$s illustrates the beginning of the modification stage. The cross-section for $t = 1200s$ shows the maximum peak height. Lastly, the cross-section for $t = 4170$s represents the state at the end of the simulation.

the end of our simulation, the impactor has penetrated the crust but remains at shallow depth within the magma ocean below a highly fragmented crust.

3.2. Resolution test

iSALE simultaneously solves the conservation equations with constitutive relations for material properties. These equations can be solved by simultaneously applying the Eulerian (grid domain) and a Lagrangian (tracers) hybrid methods. The tracers are particularly relevant for following the impactor material

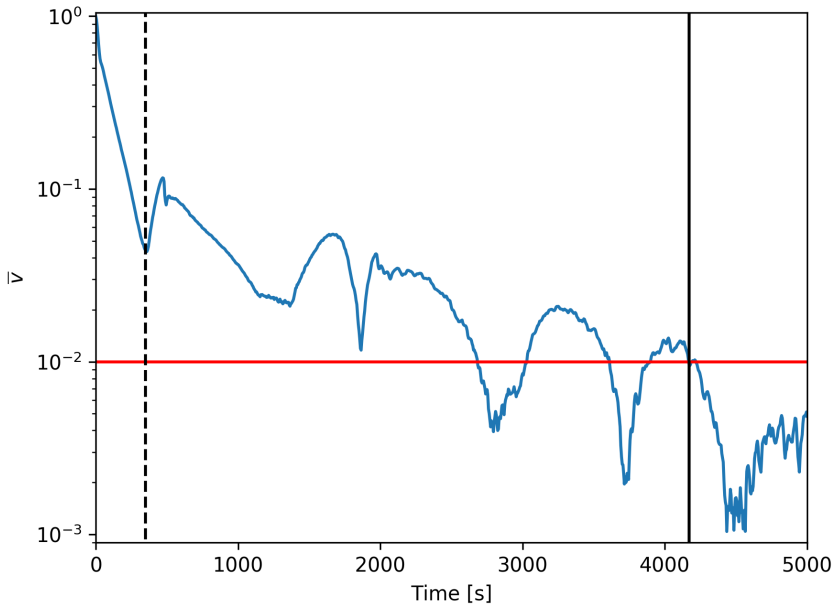

Figure 3: Temporal evolution of the average velocity of the impactor material over the initial impact velocity for the reference model ($v_{imp} = v_e = 2.33$ km s^{-1}, $\delta_{crust} = 40$ km and $R_{imp} = 50$ km). The red line represents our arbitrary stop criterion (fixed to a velocity ratio of 1%). The black dashed line represents the time of formation of the transient crater. The black solid line represents the time at which we stopped our simulation.

and for monitoring its pressure/temperature evolution as well as the maximum pressure/temperature over time. In our models, we consider a computational domain that is large enough to limit the loss of material ejected during the impact but not so extensive that it wastes computational time. Hence, the conservation equations are solved in a 10,000 km $\times$ 2000 km domain. In the following section, we define a reference case which also provides the basis for subsequent discussion on the choice of the spatial resolution.

To choose the spatial resolution of our models, we ran the reference model ($R_{imp} = 50$ km, $v_{imp} = v_e$ and $\delta_{crust} = 40$ km) at different resolutions ranging from 5 cells per projectile radius (cppr) to 50 cppr (which corresponds to a grid size ranging from 10 km to 1 km respectively). iSALE enables to use a non-uniform mesh with a resolution that is finer close to the impact site and coarser in the antipodal region of the impacted Moon where deformation is less significant. We investigated both uniform and non-uniform resolutions. Non-uniform grids are associated to the index "$_{ext}$" (i.e. cppr$_{ext}$). For this resolution test, we modeled the impact process up to 1000 s after the impact and compared the final mass from our models to the initial mass of the impactor ($m_{imp,0} = \frac{4}{3}\pi R_{imp}^3 \, \rho_{imp}$ with ρ_{imp} the impactor density). The relative average error is calculated as:

$$\epsilon(t) = \frac{(m_{imp}(t) - m_{imp,0})}{m_{imp,0}} \times 100 \tag{1}$$

with $m_{imp}(t)$ the impactor mass from our models. $\epsilon(t)$ is used as a criterion for the selection of the resolution.

For very energetic impact cases, the impactor material can potentially be buried deep within the target and may mix with the pre-existing lunar mantle.

As both the impactor and the lunar mantle are made of the same dunitic material in our model, it may be difficult to differentiate between these two materials using the Eulerian method. To overcome this problem, about one million Lagrangian tracer particles were implanted in the impactor to monitor its average depth, pressure and temperature during the impact.

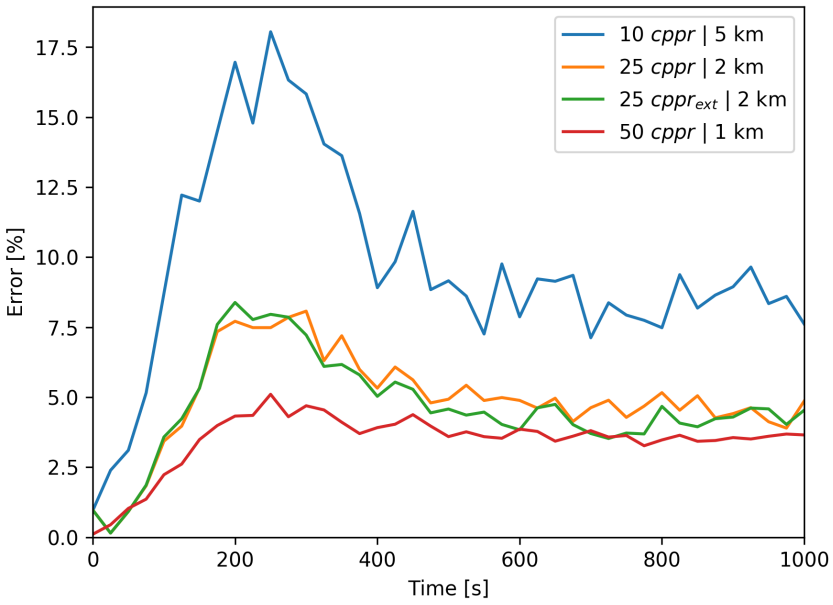

Figure 4: Time evolution of the mass error for the impactor ($\epsilon(t)$) for different spatial resolutions (see Eq. 1). Cases with 10 cppr, 25 cppr and 50 cppr have a uniform mesh. For the case with 25 cppr$_{ext}$ the resolution is non-uniform with a resolution of 25 cppr close to the impact site and half this resolution in the other parts of the planet. We consider here the reference case with $R_{imp} = 50$ km, $v_{imp} = v_e = 2.33$ km s^{-1} and $\delta_{crust} = 40$ km.

Figure 4 shows the evolution of error for different resolutions as a function of time and illustrates that the error is sensitive to the different impact stages. During the contact/compression stage, the error is lower than 2.5% for all the resolutions considered. During the excavation stage, which end up at 315 s, the error increases up to a maximal value of ≈8% for the 25 cppr$_{ext}$ resolution.

Then the error decreases until the end of the excavation stage. During the modification stage, the error varies slightly around a value of ≈5% for resolution of 25 cppr. A relatively low error is obtained during the compression stage because the impactor material experiences a density increase while concentrated in a few cells. On the contrary, during the vertical jet formation the material is dispersed in the surrounding cells and the error increases due to the numerical diffusion.

The computational time is also an important criterion to consider when choosing the resolution for our models. The computational time depends on the spatial resolution, the computational capacities, the size of the domain defined and the duration of the impact process. For the simulations detailed in our study, we used a computer with a SSD disk of 1 TB, memory 64 GB RAM and a processor Intel® Xeon(R) W-10855M CPU @ 2.80GHz ×12. Figure 5 illustrates the selection criteria with the computational time (blue) and the average error (red) as a function of the resolution in cppr. The average error decreases with an increase in resolution, while the computation time strongly increases with the increasing resolution. From 25 cppr we observe a significant increase in the calculation time along with a low error decrease. An increase in spatial resolution from 25 cppr to 50 cppr leads to only a 1.28% reduction in error, but a sevenfold increase in computation time. In Figure 5, we also show the results for cases with a non-uniform resolution which leads to a decrease in computation time of ≈43% while the mean error remains constant. To maintain a low error and a reasonable computational time we chose to run models using a resolution of 25 cppr with a non-uniform grid (see Tab. 3).

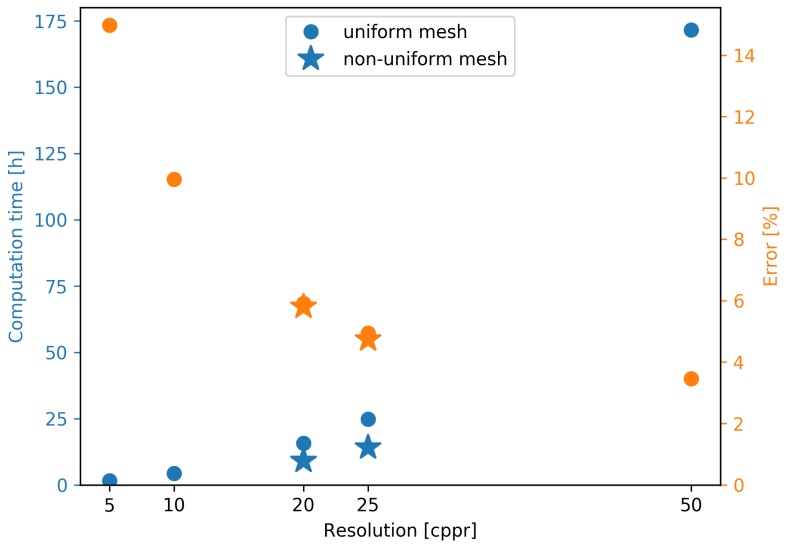

Figure 5: Computation time (blue) and error (orange) as a function of the resolution (See Eq. 1). Both values are obtained for the reference case $t = 1000$ s after the impact. The circles represent the values obtained with a uniform mesh. The stars represent the values obtained with a non-uniform mesh. For the non-uniform meshes, the resolution (in cppr) is the resolution close to the impact site while the resolution far from the impact site is half the resolution close to the impact site. We consider here the reference case with $R_{imp} = 50$ km, $v_{imp} = v_e = 2.33$ km s^{-1} km and $\delta_{crust} = 40$.

4. Fate of the impactor: parametric study

Recently, *Jackson et al.* (2023) used numerical modeling to assess the impactor's ability to penetrate through a lunar crust above a magma ocean. They explored a crustal range from 1 to 40 km, with impactor radii varying from 50 m to 15 km and impact velocities from 3 to 15 km s^{-1}. They derived scaling laws that relate the kinetic energy and the potential for lunar crust deformation and penetration. In particular, they derive a scaling law that constrain the minimum kinetic energy required for the impactor to completely perforate the crust, leaving a hole in the crust that exposes the magma ocean at the surface. In the following section, we characterise the influence of the lunar crustal thickness ($10 \leq \delta_{crust} \leq 80$ km), the impactor radius ($25 \leq R_{imp} \leq 200$ km), and

the impact velocity ($v_e \leq v_{imp} \leq 4v_e$) on the ability of an impact to bury material deep within a partially molten Moon. For that, we perform a parametric study of each parameter while keeping the other parameters fixed to appropriate values. In particular, we monitor the average depth of the impactor material using more than one million tracers for these three parameters and compare our results with the scaling law derived from *Jackson et al.* (2023). According to *Jackson et al.* (2023), we explore a range of parameters where the penetration of the impactor should be fully achieved. Videos relative to the following section illustrating the temperature and compositional evolutions during the impact are hosted within our repository file (see section 9 for access details).

4.1. Influence of the lunar crustal thickness

We evaluate the influence of the target crustal thickness (δ_{crust}) on the impactor penetration depth. According to *Wieczorek et al.* (2013), the lunar crust currently has an average thickness of ≈ 40 km with a maximum thickness of 60 km. To identify the influence of the crustal thickness, we consider a range of crustal thickness values with an upper bound value larger than the lunar crustal thickness. Here, we fix the impactor radius to 50 km and the impact velocity to $v_{imp} = v_e$.

Figure 6 (top panel) shows the depth reached by the impactor material as a function of the crustal thickness. It illustrates the depth at the end of the simulation (see Subsection 3). It shows the configuration of the impactor material when the cratering flow ceases and buoyancy forces dominate, leading to a further stage of mechanical adjustment by turbulent entrainment (not modeled here). In this figure, we consider two depths: (1) the average depth which is calculated as the average depth of all the tracers and (2) the maximum depth which represents the depth of the deepest tracer. The difference between the

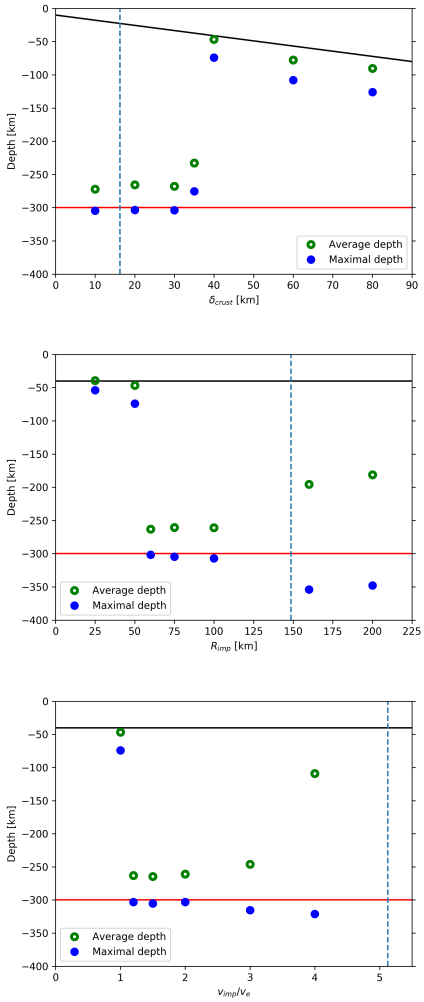

Figure 6: Final average (green symbols) and maximal (blue symbols) depth of the impactor material (top panel) as a function of the planet crustal thickness (δ_{crust}) for an impactor of radius 50 km with an impact velocity of $v_{imp} = v_e = 2.33$ km s^{-1}; (middle panel) as a function of the impactor radius R_{imp} for a crustal thickness of 40 km with an impact velocity of $v_{imp} = v_e = 2.33$ km s^{-1}; (bottom panel) as a function of the impact velocity (v_{imp}) over the escape velocity (v_e) for a crustal thickness of 40 km and an impact radius of 50 km. The red solid line corresponds to the boundary between the magma ocean and the solid mantle. The black solid line illustrates the crustal thickness of each model. The dashed blue line is the partial-complete penetration limit from *Jackson et al.* (2023)

average depth and the maximal depth illustrates the deformation and fragmentation of the impactor at the end of the impact process. We note here that we do not consider any fragmentation model in our calculations (*Wiggins et al.*, 2019). Figure 6 (top panel) also shows the thickness of the lunar crust. If the average depth is above this line, the impactor does not penetrate the crust, while below it, the impactor ends up within the magma ocean. Finally, the boundary between the magma ocean and the lower mantle is also plotted to illustrate the capacity of the impactor material to deform the deep mantle and bury the impactor material deeper than the magma ocean.

Figure 6 (top panel) shows that increasing the thickness of the crust decreases the ability of the impactor material to reach great depths within the lunar interior. For $\delta_{crust} < 30$ km, the impactor easily penetrates the crust and reaches the bottom of the magma ocean. Even if the solid mantle beneath the magma ocean acts as an efficient barrier limiting the penetration of the impactor, for $\delta_{crust} < 30$ km, we observe some tracers at depths larger than 300 km, meaning that the impactor has slightly deformed the boundary between the solid mantle and the magma ocean. For $\delta_{crust} \geq 40$ km, the impactor can still penetrate within the magma ocean but the crust strongly limits the penetration of the impactor. For these cases, in average, the impactor material finally lies beneath the crust and the final depth of the buried material increases as the crustal thickness increases. Its final position seems to be influenced by the size of the jet (see section 3) which decreases with an increase of the crust thickness.

4.2. Influence of the impactor radius

The Moon likely experienced several very large impacts during its early evolution. These large impacts probably involved impactors with radii up to 300 km

(*Bottke et al.*, 2010; *Morbidelli et al.*, 2018) while the Moon was still partially molten. Here, we evaluate the ability of a large impactor ($25 \leq R_{imp} \leq 200$ km) to penetrate through the solid crust and down into the underlying magma ocean. Here, we fix the crustal thickness to 40 km and the impact velocity to $v_{imp} = v_e$.

Figure 6 (middle panel) shows the depth reached by the impactor material as a function of the impactor radius. For $R_{imp} \leq 50$ km, the impactor penetrates the crust but the post-excavation processes and the jet dynamics tends to maintain the impactor material at shallow depths within the magma ocean (Fig. 2). For $50 < R_{imp} < 160$ km, the impactor is large enough to penetrate the crust and reaches the bottom of the magma ocean. For impactors radii larger than 160 km, a larger kinetic energy is involved which leads to greater deformation and fragmentation. For these cases, the impactor reaches the top of the solid lower lunar mantle, which acts as a mechanical barrier. Then, the impactor material spreads out within the magma ocean over a radial extent of more than 600 km and a thickness of 40 km. Ultimately, a large vertical jet is generated by the impact induced rebound which reduces the final average depth of the impactor material.

4.3. Influence of the impactor velocity

During the early stages of an impact, the kinetic energy of the impactor is rapidly transferred to the target body (*Melosh*, 1989). The available kinetic energy depends mainly on two parameters: the impactor mass (related to its radius, see section above) and the square of the impactor velocity. Hence, the impactor velocity should be a major parameter in determining the ability of the impactor to penetrate deep into the lunar interior. On the Moon, impacts can occur at a wide range of velocities. The minimum impact velocity is in the

order of the escape velocity of the Moon (v_e). Between 4.5 and 4.15 Ga, the median impactor velocity on the Moon is estimated to 9 km s^{-1} (*Bottke et al.*, 2012) and to have increased later on (*Marchi et al.*, 2012). The hypervelocity impacts ($\geq$ 10 km s^{-1}) induced by giant planet migrations are likely to have occurred during the late accretion (after 4.15 Ga) (*Marchi et al.*, 2012). The impact velocity can have a significant influence on the efficiency of the impact accretion (*Zhu et al.*, 2019a), the fragmentation of the impactor (*Kendall and Melosh*, 2016) and the melt fraction of the impactor material after the impact (*Pierazzo et al.*, 1997). In this section, we consider impact velocities ranging between 1 and 4 times the escape velocity of the impacted Moon. We fix here the crustal thickness to 40 km and the impactor radius to 50 km.

Figure 6 (bottom panel) shows that for all impact velocities considered here, the impactor penetrates the 40 km-thick crust. For $v_{imp} = v_e$ (corresponding to our reference model), the impactor material settles at shallow depth below the crust. However, for $v_{imp}/v_e > 1$, the impactor reaches the bottom of the magma ocean. In these cases, the penetration efficiency is limited by the solid lower mantle strength. Impacts with velocities larger than $3\,v_e$ deform the upper part of the solid mantle underlying the magma ocean below the impact site, enabling impactor material to penetrate below 300 km depths. For the highest impact velocities considered here, a large vertical jet is induced during the modification stage. The height of this jet increases with the impact velocity. This height can exceed 700 km above the lunar crust for the highest impact velocities. The collapse of this massive jet can transport a significant impactor fragments towards the planet surface or redistribute the fragments within the magma ocean over a wide range of depths. As a consequence, unlike the maximal depth of the impactor material, the average depth of the impactor material decreases as the

velocity increases.

4.4. Summary

For all parameter values used in our study, the impactors penetrate through the crust. For cases with a thick crust, a small impactor radius and/or a low impact velocity, the impactor material is partially buried below the lunar crust. For more energetic cases, the impactor material penetrates into the magma ocean and can be re-entrained by movements within the convecting magma ocean (*Maas et al.*, 2021). Such a secondary process is not considered in our models. *Jackson et al.* (2023) derived a scaling law characterising the impact energy threshold above which the impactor material penetrates totally within a lunar magma ocean as a function of the thickness crust. Hence, assuming a fixed impact velocity (or a fixed impactor radius), one can obtain the corresponding impactor radius (or the impact velocity) threshold separating complete and partial penetration regimes. We illustrate these values in Figure 6 (with blue dashed lines). Figure 6 (top panel) shows that the partial-complete penetration threshold obtained from our models ranges between 30 and 40 km for the crustal thickness. This value is larger but stil in agreement with the threshold thickness of 19 km derived from *Jackson et al.* (2023) scaling law. In figure 6 (middle panel), the threshold for impactor radius obtained from our models is decreased to a radius of $\sim$ 60 km compared to the value of 149 km from *Jackson et al.* (2023). Finally, figure 6 (bottom panel) shows an impactor velocity threshold of $1.1\,v_e$ which is again lower than the $5.1\,v_e$ derived from *Jackson et al.* (2023) scaling law. These results illustrate that, in our models, less impact kinetic energy is required than expected to penetrate completely through the lunar crust. This difference can be attributed to differences in the range of impactor radius (larger in our study) or to the strength properties of both the crustal and

impactor materials.

5. P, T and melt evolution of the impactor

During the impact process, the impactor material is subjected to major deformation as well as temperature and pressure modifications. Depending on the impact parameters and on the time evolution of the impact process, the impactor material can locally or globally reach the P-T conditions at which partial to complete melting occurs. To investigate whether melting is likely to occur at the surface or deep in the magma ocean, we monitor the P-T evolution of the impactor material at two specific times: the end of the excavation stage and the end of the modification stage (i.e. the end of our simulations).

5.1. Reference case

We monitored the P-T evolutions of the impactor material using one million Lagrangian tracers. Figure 7 shows the distribution of the maximum pressure and temperature reached by the population of tracers. These results are derived from the reference case described in Section 2 with $R_{imp} = 50$ km, $v_{imp} = v_e$ and $\delta_{crust} = 40$ km (see Figure 2). Two sets of histograms are illustrated in Figure 7 corresponding to the two key times specified above.

The contact/compression stage has the greatest pressure increase recorded in this reference case (up to 29 GPa). At the end of the excavation stage, following the contact/compression stage, the transient crater collapses followed by the formation of a vertical magma jet. During this second stage, which terminates at the end of the modification stage, the impactor experiences a new pressure increase, but lower than the pressure increase occurring during the contact/compression stage. This supplementary pressure increase is induced by

the inflow of material within the crater. Figure 7 (left) illustrates the maximum pressure increase experienced by the tracers during this impact process. The distribution of pressure at the end of the excavation stage is right-skewed (shifted towards a low pressure increase), while the distribution at the end of the modification stage is slightly shifted to the right. The pressure increase at the end of the excavation stage lies between 0 and 29 GPa with an average value of 5.8 GPa. At the end of the modification stage, the pressure increase ranges from 0.3 to 29 GPa with an average value of 6.1 GPa.

During the impact process, a significant fraction of the impact energy is dissipated as heat within both the impacted body and the impactor. The temperature increase within the impactor material is mainly located in the region in contact with the proto-planet (i.e. the lower surface of the impactor). The temperature increase is moderate in our reference case as the impact velocity is only 2.33 km s^{-1}. Figure 7 (right) illustrates the maximum temperature increase experienced by the tracers during the impact process. It shows that the populations before and after the modification stage are very similar. The distributions for the temperature increase at the end of the excavation stage and at the end of the modification stage are both right-skewed. During the modification stage, the crater walls collapse and the temperature may increase in the upper part of the impactor. The temperature increase at the end of the excavation stage lies between 188 and 1656 K with an average value of 605 K, whereas at the end of the modification stage the temperature increase is between 371 and 2196 K with an average value of 727 K.

From this data, we calculated the melt fraction ϕ_{melt} of the impactor material before and after the modification stage using the melting curves (solidus and

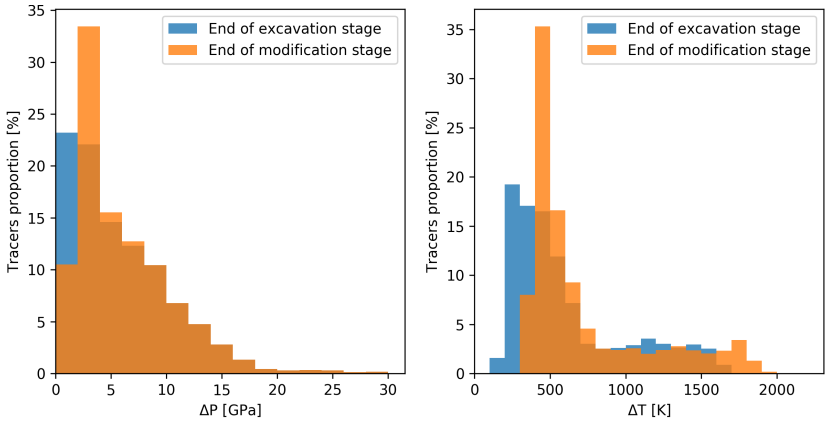

Figure 7: Maximum pressure increase (left) and maximum temperature increase (right) for each tracer in the reference model with $R_{imp} = 50$ km, $v_{imp} = 1\ v_e$ and $\delta_{crust} = 40$ km. Blue histograms corresponds to the end of the excavation stage (t=310 s), while orange histograms are obtained at the end of the modification stage (i.e. the end of the simulation with t=4170 s).

liquidus) derived for chondritic material from *Andrault et al.* (2018) for $P \leq 24$ GPa:

$$T_{sol} = 1373 \left(\frac{P}{0.82 \times 10^9} + 1 \right)^{(1/6.94)} \tag{2a}$$

$$T_{liq} = 1983.4 \left(\frac{P}{6.48 \times 10^9} + 1 \right)^{(1/5.35)} \tag{2b}$$

where T_{sol} is the solidus temperature and T_{liq} is the liquidus temperature. For $P \geq 24$ GPa, we used melting curves derived from *Andrault et al.* (2011):

$$T_{sol} = 1334.5 \left(\frac{P}{9.63 \times 10^9} + 1 \right)^{(1/2.41)} \tag{2c}$$

$$T_{liq} = 1862 \left(\frac{P}{21.15 \times 10^9} + 1 \right)^{(1/2.15)} \tag{2d}$$

Calculating the melt fraction for each tracer at each time step of our simulations, we obtained the total melt fraction within the impactor material at the end of the excavation and modification stages. For the reference case, the melt fraction is 3.87% at the end of the excavation stage and 10.17% at the end of the modification stage. Thus we can infer that, under the conditions of this reference case, the impactor melting is not significant. We then carried out a parametric study to characterise the influence of the following three parameters (δ_{crust}, R_{imp} and v_{imp}) on the ability of the impactor material to melt during the impact process. The pressure and temperature increase distributions from our models are similar to the distributions illustrated in Figure 7 (left). Histograms relative to the following section are hosted within our repository file (see section 9 for access details)

5.2. Parametric study

In Figure 8 (top panel), we illustrate the average melt fraction of the impactor as a function of the crustal thickness (δ_{crust}) at the end of both excavation and modification stages. We consider here crustal thicknesses ranging from 10 to 80 km while we fixed the impactor radius to 50 km and the impact velocity to v_e. Figure 8 (top panel) shows that the melt fraction is nearly twice larger at the end of the modification stage than at the end of the excavation stage. This means that the two stages have the same contribution to the melting fraction of the impactor. However, the thickness of the crust has a small influence on the fraction of impactor material that experiences melt. The melt fraction at the end of each simulation is lower than 16% for our whole range of δ_{crust} values. Figure 8 (top panel) illustrates that the total melt fraction decreases with in-

creasing values of δ_{crust} from 15.6 % (for $\delta_{crust} = 20$ km) to 1.2% (for $\delta_{crust} = 80$ km). For the current estimation of the lunar thickness (i.e. $\delta_{crust} \approx 40$ km), the melt fraction of the impactor at the end of the modification stage is only ≈ 10 % and the impactor material is buried in the magma ocean in a mostly solid state.

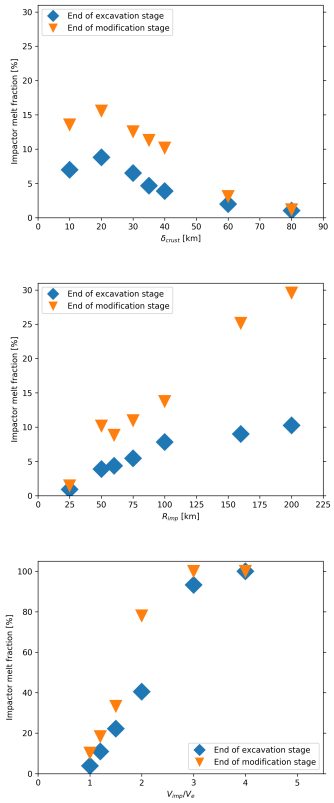

Figure 8: Average melt fraction of the impactor as a function of the crustal thickness (top panel), the impactor radius (middle panel) and the impact velocity (bottom panel). Results are obtained at the end of the excavation stage (blue) and at the end of the modification stage (orange). The material above the chondritic solidus is considered as partially molten up to the liquidus, above which it becomes fully molten.

We also investigated the melt fraction evolution of the impactor material as a function of the impactor radius (Figure 8, middle panel). We tested different values for the impactor radius ranging from 25 km to 200 km and we fixed the

crustal thickness to 40 km and the impact velocity to v_e. Figure 8 (middle panel) shows the average melt fraction of the impactor as a function of the impactor radius at the end of both the excavation and modification stages. In both cases, the impactor melt fraction increases with the impactor radius. At the end of the excavation stage, the average impactor melt fraction increases from 0.9 % to 10.2% and at the end of the modification stage, the increase ranges between 1.43 % and 29.6%. Figure 8 (middle panel) also shows that the increase is more pronounced at the end of the modification stage. This means that most of the melting process of the impactor occurs late in the impact process when the impactor material is likely to be buried below the crust within the magma ocean.

Finally, we monitored the melt fraction evolution of the impactor material as a function of the impactor velocity considering v_{imp} values between v_e and 4 v_e (Figure 8, bottom panel). Here, we fixed the crustal thickness to 40 km and the impactor radius to 50 km. Figure 8 (bottom panel) shows the average melt fraction of the impactor as a function of the impact velocity at the end of the excavation and the modification stage. Our results illustrate that the impactor velocity strongly governs the melting of the impactor material. For the lowest impact velocity, 3.9 % of the impactor has experienced melting at the end of the excavation stage and 10.2 % at the end of the modification stage. These values increase to 100% at the end of both stages for $v_{imp} = 4v_e$. Between v_e to 3 v_e, the melt fraction at the end of the excavation stage increases linearly from 3.9 % to 93.3 %. These results illustrate the sensitivity of our melting models to the impact velocity. Above a critical value $v_{imp} = 4v_e$, the impactor material is fully molten before reaching the magma ocean. The only way to envision impactor material penetrating the magma ocean without experiencing significant melt is to consider low impactor velocities close to or slightly larger

than the lunar escape velocity.

6. Impactor degassing

In the previous section, we have estimated the pressure and temperature conditions within the impactor during an impact process involving a molten layer below the Moon's crust. In the following section we make an attempt to quantify the dehydration from the impactor's material and the water partitioning between the Moon's surface and its interior.

6.1. Impact degassing criterion

The dehydration enhanced by meteoritic impacts is a complex process. According to experimental studies (*Lange and Ahrens*, 1982; *Nakato et al.*, 2008; *Nozaki et al.*, 2006), the dehydration of chondritic material is related to the destabilisation of phyllosilicates and should initiate at a temperature of ~ 873 K. *Nakato et al.* (2008) showed that phyllosilicates need to be heated at 873 K for a few days to be partly dehydrated. At 1173 K the dehydration of phyllosilicates is more efficient and occurs in less than one hour. The dehydration process is also pressure dependent. If the dehydration reaction is weakly pressure-dependent below a peak shock pressure of 21 GPa, *Sekine et al.* (2015) showed that it becomes significant at pressures ranging between 21 and 60 GPa. Their experiments suggest a full dehydration of antigorite at $T = 1073$ K. At relatively higher temperatures (up to 1500 K) forsterite dust grains are able to retain chemisorbed water at their surfaces (*King et al.*, 2010). Like the CI chondrites, the CM chondrites contain mainly serpentine minerals. Hence the CM chondrites can be considered as an analogue to the dehydration of serpentines in chondrites. *Thompson et al.* (2021) experimentally heated CM chondrites from 475 to 1475 K during a period of 5 hours. They showed that at $T = 973$ K, the partial pressure of the vaporised water decreases, but the water is still part of

the majority of the volatile compounds degassed at 973 K for more than two hours. Hence, it appears that the dehydration process enhanced by an impact strongly depends on the temperature and pressure conditions related to the impact process itself. But it also strongly depends on the chemical composition of the material involved, the main carrier phases of water, and the duration of the destabilisation process.

To understand the origin of hydrous minerals on the surface of asteroids, *Wakita and Genda* (2019) developed numerical impact models assuming a dehydration temperature of 873 K. This temperature corresponds to an absolute specific entropy of dehydration $S_{dehydr} = 3.2143$ kJ K^{-1} kg^{-1}. As illustrated in the previous sections, the impact processes occur in a very short in time. In our models, between the high pressures generated by the contact and compression stages and the modification stage where the crater walls collapse, the impactor material may be destabilised for a period of maximum 300 s. Hence it is likely that a portion of the impactor material heated at 873 K during a few minutes would not fully dehydrate. Moreover, we have illustrated in the previous sections that the peak pressure increase was strongly dependent of the impact velocity. For $v_{imp} = v_e$ and $R_{imp} = 50$ km the pressure increase reaches a maximum value of 29 GPa while for $v_{imp} = 4v_e$, the maximum pressure increase may reach a value of 121.4 GPa. As a consequence and in agreement with *Sekine et al.* (2015), it seems relevant to consider a dehydration criterion that is both a function of pressure and temperature.

Figure 9 compares the fraction of the impactor material that is dehydrated for the two discussed criterion: (1) a dehydration related to the melt fraction of chondritic material (from solidus and liquidus) and (2) the dehydration

temperature of 873 K proposed by *Wakita and Genda* (2019). For these two dehydration models, we compare the fraction of the impactor dehydrated at the end of the excavation stage (that is likely to degas within the lunar atmosphere) and at the end of the modification stage (that is likely to degas within the lunar mantle). The material that is not degassed at the end of the excavation stage should also contribute to the water content of the lunar mantle. Figure 9 shows that the fraction of the impactor material that is likely to experience dehydration is larger when considering a dehydration temperature of 873 K instead of the molten volume fraction. We observe that the difference between the two dehydration models can represent nearly 70% in particular for the cases with $v_e < v_{imp} < 2v_e$ (Figure 9, bottom) or for the cases with $R_{imp} > 150$ km (Figure 9, middle). The conditions for full dehydration are more difficult to reach assuming the melt fraction criterion. Indeed, in this case and at ambient pressure, dehydration should initiate at T=1373 K and full dehydration should occur at T=1983 K. Hence the melt fraction criterion represents a lower bound of the dehydration induced by impact while the 873 K dehydration temperature criterion represents an upper bound. Hence using the melt fraction of the impactor material as a proxy of the impactor dehydration likely overestimates the amount of water that can be buried within the magma ocean while the model proposed by *Wakita and Genda* (2019) likely overestimates the amount of surface water degassed by impact. Finally, we note that once the impactor is buried within the magma ocean, the pressure overlying the impacted material is high enough for its water to be dissolved into the magma. Hence, all the material that is not dehydrated during the impact will potentially contribute to the water content of the Moon's mantle.

Figure 9 also shows that both excavation and modification stages contribute

to the dehydration with similar contributions. For example, for $R_{imp} = 160$ km (Figure 9, middle) and assuming the melt fraction criterion, 9% of the impactor material is dehydrated during the excavation stage and 16% is dehydrated during the modification stage. This feature is also visible assuming a 873 K dehydration temperature. For $R_{imp} = 160$ km, 55% of the impactor material is dehydrated during the excavation stage and 40% is dehydrated during the modification stage. However, Figure 9 (top and middle) shows that the relative contribution from the excavation stage increases with the crust thickness while it decreases with the radius of the impactor. Hence, assuming that the excavation stage contributes to the degassing within the lunar atmosphere and the modification stage contributes to the hydratation of the lunar interior, large impacts on a thin lunar crust should favour degassing within the lunar magma ocean.

Finally, Figure 9 (bottom) shows that the impact velocity plays a key role in the degassing process. For $v_{imp} \geq 3v_e$, the impactor materiel is fully dehydrated during the excavation stage independently of the dehydration model. For these large impact velocities, all the water content from the impactor should degas at the surface of the Moon and contribute to its early atmosphere composition. However, for $1 < v_{imp} < 3v_e$, Figure 9 (bottom) shows that it is possible for the impactor material to penetrate the crust without experiencing a full dehydration. For example, for $v_{imp} = v_e$ and considering the melt fraction criterion, only 4% of the impactor is dehydrated at the end of the modification stage and 10% at the end of the modification stage. When considering a dehydration temperature of 873 K, these two values increase to 35% and 42% respectively. This means that, depending on the dehydration model, between 65% and 96% of the water content of the impactor is likely to contribute to the water budget

of the lunar interior for low velocity impacts (with $v_{imp} = v_e$).

6.2. Contribution of large impacts to the lunar water content

The mass of material accreted within the Moon's mantle after the Moon forming impact has been constrained using highly siderophile elements and the Re-Os systematics. *Day et al.* (2007) calculated a contribution of 0.02% of CI-type chondrite to the lunar mass which corresponds to 1.5×10^{19} kg. More recently it has been estimated that nearly 2.4×10^{20} kg of chondritic material have impacted the Moon during the lunar magma ocean stage (between 4.3 and 4.5 Gyr) to explain the lunar HSE budget (*Zhu et al.*, 2019a). The contribution from impactors with radii larger than 25 km can been estimated to $\approx 10\%$ of the total impactor mass (i.e. 2.4×10^{19} kg) (*Zhu et al.*, 2019a). From our models, we can estimate the fraction of a large impactor that is buried beneath the solid crust without experiencing melting during the impact process. This provides an estimation of the mass of water that can be buried within the LMO during the late lunar accretion.

We have seen in the previous sections that, in our range of parameters, a large impactor is likely to penetrate the crust and to be buried within the underlying magma ocean. If we focus on the early stages of the lunar solidification, the crustal thickness has increased with time up to its current thickness $\delta_{crust} = 40$ km (*Wieczorek et al.*, 2013). However our results show a weak influence of the lunar crust thickness on the dehydration fraction for δ_{crust} ranging between 10 and 40 km. For this range of crustal thicknesses, the dehydration fraction remains below a value of 10% (Figure 9, top). This feature also stands for the impactor radius. Degassing increases with the size of the impactor but the de-

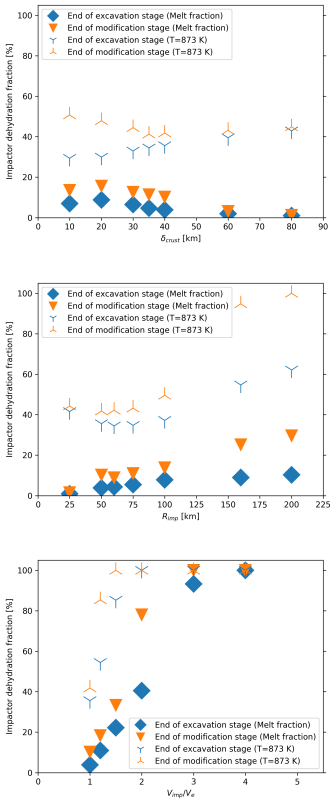

Figure 9: Fraction of the impactor experiencing dehydration as a function of the crustal thickness (top panel), the impactor radius (middle panel) and the impact velocity (bottom panel). The blue symbols represent the results obtained at the end of the excavation stage assuming the melt fraction criterion (squares) and the dehydration temperature of 873 K (crosses). The orange symbols represent the results obtained at the end of the modification stage using the melt fraction criterion (triangles) and the dehydration temperature of 873 K (crosses).

hydration fraction remains below 10% when the impactor reaches the magma ocean for $25 < R_{imp} < 200$ km (Figure 9, middle). However, our models show that (1) for $v_{imp} = 4v_e$, the impactor material is significantly molten and degassed before reaching the lunar interior and (2) for $v_{imp} = v_e$, the impactor material is mostly solid and remains hydrated when until buried below the lunar crust (Figure 9, bottom).

The potential water contribution from large and low velocity impacts within the LMO depends on the water content of the impactor. The hydrogen isotopic composition of water in lunar samples is similar to carbonaceous chondrites and addition of CI-type material has been commonly suggested (*Tartèse et al.*, 2013; *Füri et al.*, 2014). Chondrites from this group are the most enriched in terms of volatile elements (*Hauri et al.*, 2015) with a water content of 8.5 wt% for the average water concentration of a CI-type chondrite (*Piani et al.*, 2020). We consider this composition as our water-rich case. Enstatite chondrites (EC) represent the most depleted hydrogen end-member but the new calculation of H content by *Piani et al.* (2020) gives water contents ranging from 0.08 to 0.54 wt % (i.e. 800 to 5400 ppm). Then EC are not devoid of water as previously suggested and could have contributed to the endogenous lunar volatile contents during the late accretion stage. We consider this composition as our water-poor case. If 10% of the total impacted mass (i.e. 2.4×10^{20} kg, (*Zhu et al.*, 2019a)) accretes on the Moon from impactors with $R_{imp} \geq 25$ km and that 90% of this mass is trapped within the magma ocean, it represents a potential source of 1.9×10^{18} kg of water (for the water-rich case) and 1.8×10^{16} to 1.22×10^{17} kg of water (for the water-poor case) in this molten reservoir. The water contribution can be lower for differentiated impactors (divided by a factor 3 for EC aubrite)

Assuming a 100 km-thick lunar magma ocean below a 40 km-crust, the mass of the magma ocean is 1.14×10^{22} kg. If the magma ocean is initially depleted in water, the water content after this late accretive event could vary between 168.7 ppm (for the water-rich case) and from 1.6 ppm (for the water-poor case with water concentration of 0.08 wt%) to 10.7 ppm (for the water-poor case with water concentration of 0.54 wt%) for EC. For the water-poor case, we obtain water concentrations consistent with estimations proposed for the lunar mantle source (i.e. 1.2 to 74 ppm of water, (*McCubbin et al.*, 2023)). The water concentration calculated using the water-rich case exceeds the water concentration estimated in the bulk silicate Moon from lunar sample measurements. Our estimations can easily be reconciled with the measurements if only 5% of the total impacted mass comes from impactors with $R_{imp} \geq 25km$.

Finally, for the consistency of our scenario, two features have to be accounted for: (1) the ability of the accreted material to be fully homogenised within the LMO or (2) the ability of this material to be distributed within the mantle so that it can be sampled statistically. We note that, in this scenario, the total mass accreted from impactors with $R_{imp} \geq 25km$ represents the mass of $\approx$ 100 impactors with $R_{imp} = 25$ km or a single impactor with $R_{imp} = 125$ km. If full chemical homogenisation is likely in the LMO then the water content can be explained by a single 125 km radius impact made of water-rich material. However, such a chemical homogenisation within a thin LMO is difficult to imagine because of the lack of vigorous convection. Moreover, such a scenario would be difficult to reconcile with the apparent water content heterogeneities found in the lunar samples. Complementary models are needed to explore this point which is beyond the scope of our study. A late delivery

of water by 100 large water-poor impacts into the lunar interior would help reconcile the different water estimates because such a process would probably favour large chemical heterogeneities in the lunar interior. Morevover, to favor a heterogenous water content in the lunar mantle, it is likely that impactors of different origins contributed to the water budget of the lunar mantle during its late accretion.

7. Discussion

Our models represent a first attempt to constrain the mass of impactor material that could be accreted deep within the early Moon following a large impact and in particular how the impactor material could be trapped within the residual LMO located below a thick crust. As a first step, several simplifying assumptions have been made. Among these simplifications, not accounting for the porosity effects is likely to be the most important assumption since large range of values may be found among the different types of chondrites. For example, measurements made on CI chondrites show porosity values of ≈30% (*Ostrowski and Bryson*, 2019). However, *Davison et al.* (2010) show that it is easier to melt porous impactors. Not accounting for the porosity may lead to an underestimation of the fraction of the molten material during an impact. This effect is limited in the cases of our study since we consider relatively low impact velocities. However, in future models, when considering larger and probably more plausible impact velocities, the porosity effects have to be accounted for.

Once the impactor material is buried within the magma ocean, its capacity to be homogenised within the magma ocean depends on the mixing dynamics of the magma ocean. The vigor of the convection is essentially governed by the viscosity and thickness of the magma ocean. Thus the post-accretionary

homogenisation of the impactor material and its volatile content within the magma ocean are, governed by the cooling efficiency of the early Moon. To better constrain the fate of the impactor material during a large impact and a large accretionary event, we need to carry out 3D models. Such models are much more costly in terms of computational time but could strongly constrain the influence of the impact angle on the ability of the impact to bury material deep within the early Moon and on the fragmentation efficiency. Depending on fragmentation of the impactor, the homogenisation could be partial or complete (small impactor). A weak homogenisation of the LMO could potentially explain the heterogeneous distribution of volatiles in the lunar interior. This aspect is beyond the scope of this study and requires dedicated models.

There is no evidence of cratering during the magma ocean period. The impact craters fade away due to thermal relaxation at high temperature (*Miljković et al.*, 2021) and the HSE partitioned into the lunar core (*Morbidelli et al.*, 2018). Late accretion is considered to be highly stochastic (*Bottke et al.*, 2010) but the timing of impacts has a bearing on the potential for burying hydrated material. It is easier to bury small impactors when the crust is thin, and then to homogenise them later. As the crust becomes thicker, the critical impactor size needed to perforate it increases and the homogenisation of the buried material within a thin magma ocean is more difficult. An approach coupling lunar thermal evolution, solidification processes and late accretionary events would strongly enhance our understanding of the chemical composition of the lunar samples.

Finally, our results show that a significant part of the impactor material is molten during the impact for $v_{imp} \geq 2v_e$ (Figure 9, bottom). As a consequence

its water content may lost into the lunar atmosphere following the impact. This loss may help resolve inconsistent results for considering HSE and H measurements. Our study focuses on low velocity impacts while high velocity impacts are probably more likely at the end of the lunar accretion. Hence we now need to understand the evolution of this lunar atmosphere (*Saxena et al.*, 2017) and the contribution of the large impacts to its erosion.

8. Conclusion

We developed hydrocode simulations with iSALE 2D to monitor the ability of a large impactor to bury material within a partially molten lunar body. We investigated the influence of crustal thickness (from 10 to 80 km), impactor radius (from 25 to 200 km) and impact velocity (from v_e to $4v_e$) on the potential contribution of these large impactors on the water budget of the lunar mantle. We evaluated the impactor melt fraction assuming chondritic material to determine the fraction of devolatilised material before penetration into the LMO below the solid crust. Our results show that impactors with radii larger than 25 km are likely to penetrate the crust overlying the lunar magma ocean for impact velocities larger than the lunar escape velocity. If the impact velocity is higher than $3v_e$, complete melting and devolatilisation of the impactor are achieved. For these high velocity cases, the volatile content would contribute to the volatile budget of the early Moon's atmosphere. However, low impact velocities ($\approx v_e$) favour the penetration of the impactor material into the lunar mantle without experiencing significant melt and impact dehydration. For these cases, at least 90% of the impactors mass may contribute to the volatile budget of the lunar mantle.

The mass of late accreted material is commonly calculated using results from HSE measurements. We calculated the concentration of water within a homogenised magma ocean after an accretionary event consisting of 2.4×10^{20} kg of chondritic material. We assumed the contribution from two end-member types of chondrite : EC (water-poor) and CI (water-rich). The water concentration in a homogeneous post-accretion mantle would be 1.6 to 10.7 ppm for a water-poor case and 168.7 ppm for a water-rich one. Such an accretionary event is likely to favour a heterogeneous distribution of volatiles in the lunar interior. If post-accretion homogenisation is not achieved, the late delivery of volatile elements by impacts could explain the large range of H concentration measured in apatites from different lunar rock types (*McCubbin et al.*, 2023).

9. Data availability

The extended data and data analysis from numerical simulations generated in this study are accessible via `https://doi.org/10.25519/6PHB-FV69` The iSALE-2D input files used to generate simulations are also available and been deposited in the same database.

Acknowledgements

The authors deeply thank Ross Potter, Meng-Hua Zhu and the editor Brandon Johnson for their constructive reviews. The authors thank Francis McCubbin for having shared his compilations on lunar volatile elements. We also thank Yves Marrocchi for useful discussions. We gratefully acknowledge the developers of iSALE-2D, including Gareth Collins, Kai Wünnemann, Dirk Elbeshausen, Tom Davison, Boris Ivanov and Jay Melosh. Some plots in this work were created with the pySALEPlot tool written by Tom Davison. This research re-

ceived funding from the french government Laboratory of Excellence initiative No. ANR-10-LABX-0006 (Labex ClerVolc) and from the French PNP program (INSU-CNRS). This is ClerVolc contribution number 648. We thank Frances van Wyk de Vries for english editing of this article.

References

Agnor, C., and E. Asphaug (2004), Accretion Efficiency during Planetary Collisions, *The Astrophysical Journal*, *613*(2), L157–L160, doi:10.1086/425158.

Amsden, A. A., H. M. Ruppel, and C. W. Hirt (1980), SALE: a simplified ALE computer program for fluid flow at all speeds, *Tech. Rep. LA-8095*, Los Alamos Scientific Lab., NM (USA), doi:10.2172/5176006.

Andrault, D., N. Bolfan-Casanova, G. L. Nigro, M. A. Bouhifd, G. Garbarino, and M. Mezouar (2011), Solidus and liquidus profiles of chondritic mantle: Implication for melting of the Earth across its history, *Earth and Planetary Science Letters*, *304*(1), 251–259, doi:10.1016/j.epsl.2011.02.006.

Andrault, D., G. Pesce, G. Manthilake, J. Monteux, N. Bolfan-Casanova, J. Chantel, D. Novella, N. Guignot, A. King, J.-P. Itié, and L. Hennet (2018), Deep and persistent melt layer in the Archaean mantle, *Nature Geoscience*, *11*(2), 139–143, doi:10.1038/s41561-017-0053-9.

Andrews-Hanna, J. C., J. Besserer, J. W. Head III, C. J. A. Howett, W. S. Kiefer, P. J. Lucey, P. J. McGovern, H. J. Melosh, G. A. Neumann, R. J. Phillips, P. M. Schenk, D. E. Smith, S. C. Solomon, and M. T. Zuber (2014), Structure and evolution of the lunar Procellarum region as revealed by GRAIL gravity data, *Nature*, *514*(7520), 68–71, doi:10.1038/nature13697, number: 7520 Publisher: Nature Publishing Group.

Artemieva, N. (2007), Possible reasons of shock melt deficiency in the Bosumtwi drill cores, *Meteoritics and Planetary Science*, *42*(4), 883–894, doi:10.1111/j.1945-5100.2007.tb01083.x.

Barnes, J. J., D. A. Kring, R. Tartèse, I. A. Franchi, M. Anand, and S. S. Russell (2016), An asteroidal origin for water in the Moon, *Nature Communications*, *7*(1), 11,684, doi:10.1038/ncomms11684, number: 1.

Benz, W., A. Cameron, and H. Melosh (1989), The origin of the Moon and the single-impact hypothesis III, *Icarus*, *81*(1), 113–131, doi:10.1016/0019-1035(89)90129-2.

Borg, L. E., G. A. Brennecka, and T. S. Kruijer (2022), The origin of volatile elements in the Earth–Moon system, *Proceedings of the National Academy of Sciences*, *119*(8), e2115726,119, doi:10.1073/pnas.2115726119.

Bottke, W. F., A. Cellino, P. Paolicchi, and R. P. Binzel (Eds.) (2002), *Asteroids III*, University of Arizona Press, doi:10.2307/j.ctv1v7zdn4.

Bottke, W. F., R. J. Walker, J. M. Day, D. Nesvorny, and L. Elkins-Tanton (2010), Stochastic Late Accretion to Earth, the Moon, and Mars, *Science*, *330*(6010), 1527–1530, doi:10.1126/science.1196874.

Bottke, W. F., D. Vokrouhlický, D. Minton, D. Nesvorný, A. Morbidelli, R. Brasser, B. Simonson, and H. F. Levison (2012), An Archaean heavy bombardment from a destabilized extension of the asteroid belt, *Nature*, *485*(7396), 78–81, doi:10.1038/nature10967.

Boyce, J. W., A. H. Treiman, Y. Guan, C. Ma, J. M. Eiler, J. Gross, J. P. Greenwood, and E. M. Stolper (2015), The chlorine isotope fingerprint of the lunar magma ocean, *Science Advances*, *1*(8), e1500,380, doi:10.1126/sciadv.1500380.

1181 Bray, V. J., G. S. Collins, J. V. Morgan, H. J. Melosh, and P. M. Schenk (2014),
1182 Hydrocode simulation of Ganymede and Europa cratering trends – How thick
1183 is Europa's crust?, *Icarus*, *231*, 394–406, doi:10.1016/j.icarus.2013.12.009.

1184 Bruck Syal, M., and P. H. Schultz (2015), Cometary impact effects at the Moon:
1185 Implications for lunar swirl formation, *Icarus*, *257*, 194–206, doi:10.1016/j.
1186 icarus.2015.05.005.

1187 Cameron, A. G. W., and W. R. Ward (1976), The Origin of the Moon, *Lunar*
1188 *and Planetary Science Conference*, *7*, 120.

1189 Canup, R. (2008), Lunar-forming collisions with pre-impact rotation, *Icarus*,
1190 *196*(2), 518–538, doi:10.1016/j.icarus.2008.03.011.

1191 Canup, R. M. (2004), Simulations of a late lunar-forming impact, *Icarus*, *168*(2),
1192 433–456, doi:10.1016/j.icarus.2003.09.028.

1193 Canup, R. M. (2012), Forming a Moon with an Earth-like Composition via a
1194 Giant Impact, *Science*, *338*(6110), 1052–1055, doi:10.1126/science.1226073.

1195 Charlier, B., T. L. Grove, O. Namur, and F. Holtz (2018), Crystallization of
1196 the lunar magma ocean and the primordial mantle-crust differentiation of the
1197 Moon, *Geochimica et Cosmochimica Acta*, *234*, 50–69, doi:10.1016/j.gca.2018.
1198 05.006.

1199 Collins, G. S. (2014), Numerical simulations of impact crater formation with
1200 dilatancy, *Journal of Geophysical Research (Planets)*, *119*(12), 2600–2619,
1201 doi:10.1002/2014JE004708.

1202 Collins, G. S., H. J. Melosh, and B. A. Ivanov (2004), Modeling damage and
1203 deformation in impact simulations, *Meteoritics & Planetary Science*, *39*(2),
1204 217–231, doi:10.1111/j.1945-5100.2004.tb00337.x.

1205 Collins, G. S., H. J. Melosh, and G. R. Osinski (2012), The Impact-Cratering
1206 Process, *Elements*, *8*(1), 25–30, doi:10.2113/gselements.8.1.25.

1207 Collins, G. S., D. Elbeshausen, K. Wünnemann, T. M. Davison, B. Ivanov,
1208 and H. J. Melosh (2016), iSALE: A multi-material, multi-rheology shock
1209 physics code for simulating impact phenomena in two and three dimen-
1210 sions, *Manual for the Dellen release of the iSALE shock physics code*, doi:
1211 10.6084/m9.figshare.3473690.

1212 Ćuk, M., and S. T. Stewart (2012), Making the Moon from a Fast-
1213 Spinning Earth: A Giant Impact Followed by Resonant Despinning, *Science*,
1214 *338*(6110), 1047, doi:10.1126/science.1225542.

1215 Davison, T., G. Collins, and F. Ciesla (2010), Numerical modelling of heating in
1216 porous planetesimal collisions, *Icarus*, *208*(1), 468–481, doi:10.1016/j.icarus.
1217 2010.01.034.

1218 Day, J. M. D., D. G. Pearson, and L. A. Taylor (2007), Highly Siderophile Ele-
1219 ment Constraints on Accretion and Differentiation of the Earth-Moon System,
1220 *Science*, *315*(5809), 217–219, doi:10.1126/science.1133355.

1221 Elbeshausen, D., K. Wünnemann, and G. S. Collins (2009), Scaling of oblique
1222 impacts in frictional targets: Implications for crater size and formation mech-
1223 anisms, *Icarus*, *204*(2), 716–731, doi:10.1016/j.icarus.2009.07.018.

1224 Elkins-Tanton, L. T., S. Burgess, and Q.-Z. Yin (2011), The lunar magma ocean:
1225 Reconciling the solidification process with lunar petrology and geochronology,
1226 *Earth and Planetary Science Letters*, *304*(3-4), 326–336, doi:10.1016/j.epsl.
1227 2011.02.004.

1228 Evans, A. J., J. C. Andrews-Hanna, J. W. Head III, J. M. Soderblom, S. C.
1229 Solomon, and M. T. Zuber (2018), Reexamination of Early Lunar Chronology

With GRAIL Data: Terranes, Basins, and Impact Fluxes, *Journal of Geophysical Research: Planets*, *123*(7), 1596–1617, doi:10.1029/2017JE005421.

Füri, E., E. Deloule, A. Gurenko, and B. Marty (2014), New evidence for chondritic lunar water from combined D/H and noble gas analyses of single Apollo 17 volcanic glasses, *Icarus*, *229*, 109–120, doi:10.1016/j.icarus.2013.10.029.

Füri, E., E. Deloule, A. Gurenko, and B. Marty (2014), New evidence for chondritic lunar water from combined D/H and noble gas analyses of single Apollo 17 volcanic glasses, *Icarus*, *229*, 109–120, doi:10.1016/j.icarus.2013.10.029.

Garcia, R. F., J. Gagnepain-Beyneix, S. Chevrot, and P. Lognonné (2011), Very preliminary reference Moon model, *Physics of the Earth and Planetary Interiors*, *188*(1-2), 96–113, doi:10.1016/j.pepi.2011.06.015.

Garrick-Bethell, I., and M. T. Zuber (2009), Elliptical structure of the lunar South Pole-Aitken basin, *Icarus*, *204*(2), 399–408, doi:10.1016/j.icarus.2009.05.032.

Hartmann, W. K., and D. R. Davis (1975), Satellite-sized planetesimals and lunar origin, *Icarus*, *24*(4), 504–515, doi:10.1016/0019-1035(75)90070-6.

Hauri, E. H., A. E. Saal, M. J. Rutherford, and J. A. Van Orman (2015), Water in the Moon's interior: Truth and consequences, *Earth and Planetary Science Letters*, *409*, 252–264, doi:10.1016/j.epsl.2014.10.053.

Hosono, N., S.-i. Karato, J. Makino, and T. R. Saitoh (2019), Terrestrial magma ocean origin of the Moon, *Nature Geoscience*, *12*(6), 418–423, doi:10.1038/s41561-019-0354-2.

Hu, S., H. He, J. Ji, Y. Lin, H. Hui, M. Anand, R. Tartèse, Y. Yan, J. Hao, R. Li, L. Gu, Q. Guo, H. He, and Z. Ouyang (2021), A dry lunar mantle

reservoir for young mare basalts of Chang'e-5, *Nature*, *600*(7887), 49–53, doi:10.1038/s41586-021-04107-9.

Ito, T., and R. Malhotra (2010), Asymmetric impacts of near-Earth asteroids on the Moon, *Astron. and Astroph.*, *519*, A63, doi:10.1051/0004-6361/200912901.

Ivanov, B., D. Deniem, and G. Neukum (1997), Implementation of dynamic strength models into 2D hydrocodes: Applications for atmospheric breakup and impact cratering, *International Journal of Impact Engineering*, *20*(1-5), 411–430, doi:10.1016/S0734-743X(97)87511-2.

Ivanov, B., H. Melosh, and E. Pierazzo (2010), Basin-forming impacts: Reconnaissance modeling, in *Large Meteorite Impacts and Planetary Evolution IV*, vol. 465, edited by R. L. Gibson and W. U. Reimold, p. 0, Geological Society of America, doi:10.1130/2010.2465(03).

Jackson, A. P., V. Perera, and T. S. J. Gabriel (2023), Impact Generation of Holes in the Early Lunar Crust: Scaling Relations, *Journal of Geophysical Research: Planets*, *128*(4), e2022JE007,498, doi:10.1029/2022JE007498.

James, P. B., D. E. Smith, P. K. Byrne, J. D. Kendall, H. J. Melosh, and M. T. Zuber (2019), Deep Structure of the Lunar South Pole-Aitken Basin, *Geophysical Research Letters*, *46*(10), 5100–5106, doi:10.1029/2019GL082252.

Johnson, B. C., J. C. Andrews-Hanna, G. S. Collins, A. M. Freed, H. J. Melosh, and M. T. Zuber (2018), Controls on the Formation of Lunar Multiring Basins, *Journal of Geophysical Research: Planets*, *123*(11), 3035–3050, doi:10.1029/2018JE005765.

Johnson, T., L. Morrissey, A. Nemchin, N. Gardiner, and J. Snape (2021), The phases of the Moon: Modelling crystallisation of the lunar magma ocean

through equilibrium thermodynamics, *Earth and Planetary Science Letters*, *556*, 116,721, doi:10.1016/j.epsl.2020.116721.

Jones, M. J., A. J. Evans, B. C. Johnson, M. B. Weller, J. C. Andrews-Hanna, S. M. Tikoo, and J. T. Keane (2022), A South Pole–Aitken impact origin of the lunar compositional asymmetry, *Science Advances*, *8*(14), eabm8475, doi:10.1126/sciadv.abm8475, publisher: American Association for the Advancement of Science.

Kamata, S., S. Sugita, Y. Abe, Y. Ishihara, Y. Harada, T. Morota, N. Namiki, T. Iwata, H. Hanada, H. Araki, K. Matsumoto, E. Tajika, K. Kuramoto, and F. Nimmo (2015), The relative timing of Lunar Magma Ocean solidification and the Late Heavy Bombardment inferred from highly degraded impact basin structures, *Icarus*, *250*, 492–503, doi:10.1016/j.icarus.2014.12.025.

Kendall, J. D., and H. Melosh (2016), Differentiated planetesimal impacts into a terrestrial magma ocean: Fate of the iron core, *Earth and Planetary Science Letters*, *448*, 24–33, doi:10.1016/j.epsl.2016.05.012.

King, H., M. Stimpfl, P. Deymier, M. Drake, C. Catlow, A. Putnis, and N. de Leeuw (2010), Computer simulations of water interactions with low-coordinated forsterite surface sites: Implications for the origin of water in the inner solar system, *Earth and Planetary Science Letters*, *300*(1-2), 11–18, doi:10.1016/j.epsl.2010.10.019.

Kokubo, E., and H. Genda (2010), Formation of terrestrial planets from protoplanets under a realistic accretion condition, *The Astrophysical Journal Letters*, *714*(1), L21, doi:10.1088/2041-8205/714/1/L21.

Kraettli, G., M. W. Schmidt, and C. Liebske (2022), Fractional crystallization of a basal lunar magma ocean: A dense melt-bearing garnetite layer above the core?, *Icarus*, *371*, 114,699, doi:10.1016/j.icarus.2021.114699.

Kurosawa, K., and H. Genda (2018), Effects of Friction and Plastic Deformation in Shock-Comminuted Damaged Rocks on Impact Heating, *Geophysical Research Letters*, *45*(2), 620–626, doi:10.1002/2017GL076285.

Kurosawa, K., H. Genda, S. Azuma, and K. Okazaki (2021), The Role of Post Shock Heating by Plastic Deformation During Impact Devolatilization of Calcite ($CaCO_3$), *Geophys. Res. Lett.*, *48*(7), e91130, doi:10.1029/2020GL091130.

Landeau, M., R. Deguen, D. Phillips, J. A. Neufeld, V. Lherm, and S. B. Dalziel (2021), Metal-silicate mixing by large Earth-forming impacts, *Earth and Planetary Science Letters*, *564*, 116,888, doi:10.1016/j.epsl.2021.116888.

Lange, M. A., and T. J. Ahrens (1982), Impact induced dehydration of serpentine and the evolution of planetary atmospheres, *Journal of Geophysical Research: Solid Earth*, *87*(S01), A451–A456, doi:10.1029/JB087iS01p0A451.

Le Feuvre, M., and M. A. Wieczorek (2011), Nonuniform cratering of the Moon and a revised crater chronology of the inner Solar System, *Icarus*, *214*(1), 1–20, doi:10.1016/j.icarus.2011.03.010.

Liu, W., Y. Zhang, F. L. H. Tissot, G. Avice, Z. Ye, and Q.-Z. Yin (2023), I/Pu reveals Earth mainly accreted from volatile-poor differentiated planetesimals, *Science Advances*, *9*(27), eadg9213, doi:10.1126/sciadv.adg9213.

Lock, S. J., S. T. Stewart, M. I. Petaev, Z. Leinhardt, M. T. Mace, S. B. Jacobsen, and M. Cuk (2018), The Origin of the Moon Within a Terrestrial Synestia, *Journal of Geophysical Research: Planets*, *123*(4), 910–951, doi:10.1002/2017JE005333.

Lorenz, C. A., A. I. Buikin, A. A. Shiryaev, and O. V. Kuznetsova (2021), Composition and origin of the volatile components released from the Pesyanoe

aubrite by stepwise crushing and heating, *Chemie der Erde / Geochemistry*, *81*(1), 125,686, doi:10.1016/j.chemer.2020.125686.

Lunar Sample Preliminary Examination Team (1969), Preliminary Examination of Lunar Samples from Apollo 11: A physical, chemical, mineralogical, and biological analysis of 22 kilograms of lunar rocks and fines., *Science*, *165*(3899), 1211–1227.

Luo, X.-Z., M.-H. Zhu, and M. Ding (2022), Ejecta Pattern of Oblique Impacts on the Moon From Numerical Simulations, *Journal of Geophysical Research (Planets)*, *127*(11), e2022JE007333, doi:10.1029/2022JE007333.

Maas, C., L. Manske, K. Wünnemann, and U. Hansen (2021), On the fate of impact-delivered metal in a terrestrial magma ocean, *Earth and Planetary Science Letters*, *554*, 116,680, doi:10.1016/j.epsl.2020.116680.

Manske, L., S. Marchi, A.-C. Plesa, and K. Wünnemann (2021), Impact melting upon basin formation on early Mars, *Icarus*, *357*, 114128, doi:10.1016/j.icarus.2020.114128.

Manske, L., K. Wünnemann, and K. Kurosawa (2022), Quantification of Impact-Induced Melt Production in Numerical Modeling Revisited, *Journal of Geophysical Research (Planets)*, *127*(12), e2022JE007426, doi:10.1029/2022JE007426.

Marchi, S., S. Mottola, G. Cremonese, M. Massironi, and E. Martellato (2009), A NEW CHRONOLOGY FOR THE MOON AND MERCURY, *The Astronomical Journal*, *137*(6), 4936–4948, doi:10.1088/0004-6256/137/6/4936.

Marchi, S., W. F. Bottke, D. A. Kring, and A. Morbidelli (2012), The onset of the lunar cataclysm as recorded in its ancient crater populations, *Earth and Planetary Science Letters*, *325-326*, 27–38, doi:10.1016/j.epsl.2012.01.021.

Marchi, S., R. M. Canup, and R. J. Walker (2018), Heterogeneous delivery of silicate and metal to the Earth by large planetesimals, *Nature Geoscience*, *11*(1), 77–81, doi:10.1038/s41561-017-0022-3.

Maurice, M., N. Tosi, S. Schwinger, D. Breuer, and T. Kleine (2020), A long-lived magma ocean on a young Moon, *Science Advances*, *6*(28), eaba8949, doi:10.1126/sciadv.aba8949.

McCubbin, F. M., J. J. Barnes, P. Ni, H. Hui, R. L. Klima, D. Burney, J. M. D. Day, T. Magna, J. W. Boyce, R. Tartèse, K. E. V. Kaaden, E. Steenstra, S. M. Elardo, R. A. Zeigler, M. Anand, and Y. Liu (2023), Endogenous Lunar Volatiles, *Reviews in Mineralogy & Geochemistry (New Views of the Moon-2)*, p. 56.

Melosh, H., J. Kendall, B. Horgan, B. Johnson, T. Bowling, P. Lucey, and G. Taylor (2017), South Pole–Aitken basin ejecta reveal the Moon's upper mantle, *Geology*, *45*(12), 1063–1066, doi:10.1130/G39375.1.

Melosh, H. J. (1989), Impact cratering: A geologic process, *New York: Oxford University Press; Oxford: Clarendon Press.*

Melosh, H. J., E. V. Ryan, and E. Asphaug (1992), Dynamic fragmentation in impacts: Hydrocode simulation of laboratory impacts, *Journal of Geophysical Research*, *97*(E9), 14,735–14,759, doi:10.1029/92JE01632.

Melosh, H. J., A. M. Freed, B. C. Johnson, D. M. Blair, J. C. Andrews-Hanna, G. A. Neumann, R. J. Phillips, D. E. Smith, S. C. Solomon, M. A. Wieczorek, and M. T. Zuber (2013), The Origin of Lunar Mascon Basins, *Science*, *340*(6140), 1552–1555, doi:10.1126/science.1235768.

Michaut, C., and J. A. Neufeld (2022), Formation of the Lunar Primary Crust

From a Long-Lived Slushy Magma Ocean, *Geophys. Res. Lett.*, *49*(2), e95408, doi:10.1029/2021GL095408.

Miljković, K., M. A. Wieczorek, M. Laneuville, A. Nemchin, P. A. Bland, and M. T. Zuber (2021), Large impact cratering during lunar magma ocean solidification, *Nature Communications*, *12*(1), 5433, doi:10.1038/s41467-021-25818-7.

Monteux, J., and J. Arkani-Hamed (2019), Shock wave propagation in layered planetary interiors: Revisited, *Icarus*, *331*, 238–256, doi:10.1016/j.icarus.2019.05.016.

Monteux, J., G. Tobie, G. Choblet, and M. Le Feuvre (2014), Can large icy moons accrete undifferentiated?, *Icarus*, *237*, 377–387, doi:10.1016/j.icarus.2014.04.041.

Monteux, J., D. Andrault, and H. Samuel (2016a), On the cooling of a deep terrestrial magma ocean, *Earth and Planetary Science Letters*, *448*, 140–149, doi:10.1016/j.epsl.2016.05.010.

Monteux, J., G. S. Collins, G. Tobie, and G. Choblet (2016b), Consequences of large impacts on Enceladus' core shape, *Icarus*, *264*, 300–310, doi:10.1016/j.icarus.2015.09.034.

Morbidelli, A., D. Nesvorny, V. Laurenz, S. Marchi, D. Rubie, L. Elkins-Tanton, M. Wieczorek, and S. Jacobson (2018), The timeline of the lunar bombardment: Revisited, *Icarus*, *305*, 262–276, doi:10.1016/j.icarus.2017.12.046.

Nakajima, M., and D. J. Stevenson (2018), Inefficient volatile loss from the Moon-forming disk: Reconciling the giant impact hypothesis and a wet Moon, *Earth and Planetary Science Letters*, *487*, 117–126, doi:10.1016/j.epsl.2018.01.026.

Nakamura, R., S. Yamamoto, T. Matsunaga, Y. Ishihara, T. Morota, T. Hiroi, H. Takeda, Y. Ogawa, Y. Yokota, N. Hirata, M. Ohtake, and K. Saiki (2012), Compositional evidence for an impact origin of the Moon's Procellarum basin, *Nature Geoscience*, *5*(11), 775–778, doi:10.1038/ngeo1614.

Nakato, A., T. Nakamura, F. Kitajima, and T. Noguchi (2008), Evaluation of dehydration mechanism during heating of hydrous asteroids based on mineralogical and chemical analysis of naturally and experimentally heated CM chondrites, *Earth, Planets and Space*, *60*(8), 855–864, doi:10.1186/BF03352837.

Nesvorný, D., F. V. Roig, D. Vokrouhlický, W. F. Bottke, S. Marchi, A. Morbidelli, and R. Deienno (2023), Early bombardment of the moon: Connecting the lunar crater record to the terrestrial planet formation, *Icarus*, *399*, 115545, doi:10.1016/j.icarus.2023.115545.

Nozaki, W., T. Nakamura, and T. Noguchi (2006), Bulk mineralogical changes of hydrous micrometeorites during heating in the upper atmosphere at temperatures below 1000 °c, *Meteoritics & Planetary Science*, *41*(7), 1095–1114, doi:10.1111/j.1945-5100.2006.tb00507.x.

Ostrowski, D., and K. Bryson (2019), The physical properties of meteorites, *Planetary and Space Science*, *165*, 148–178, doi:10.1016/j.pss.2018.11.003.

Palme, H., J. W. Larimer, and M. E. Lipschutz (1988), Moderately volatile elements., in *Meteorites and the Early Solar System*, edited by J. F. Kerridge and M. S. Matthews, pp. 436–461.

Perera, V., A. P. Jackson, L. T. Elkins-Tanton, and E. Asphaug (2018), Effect of Reimpacting Debris on the Solidification of the Lunar Magma Ocean, *Journal of Geophysical Research (Planets)*, *123*(5), 1168–1191, doi:10.1029/2017JE005512.

Piani, L., Y. Marrocchi, T. Rigaudier, L. G. Vacher, D. Thomassin, and z. Marty (2020), Earth's water may have been inherited from material similar to enstatite chondrite meteorites, *Science*, *369*(6507), 1110–1113, doi:10.1126/science.aba1948.

Pierazzo, E., and H. J. Melosh (2000a), Melt Production in Oblique Impacts, *Icarus*, *145*(1), 252–261, doi:10.1006/icar.1999.6332.

Pierazzo, E., and H. J. Melosh (2000b), Hydrocode modeling of oblique impacts: The fate of the projectile, *Meteoritics & Planetary Science*, *35*(1), 117–130, doi:10.1111/j.1945-5100.2000.tb01979.x.

Pierazzo, E., A. Vickery, and H. Melosh (1997), A Reevaluation of Impact Melt Production, *Icarus*, *127*(2), 408–423, doi:10.1006/icar.1997.5713.

Potter, R., G. Collins, W. Kiefer, P. McGovern, and D. Kring (2012), Constraining the size of the South Pole-Aitken basin impact, *Icarus*, *220*(2), 730–743, doi:10.1016/j.icarus.2012.05.032.

Potter, R. W. K., and G. S. Collins (2013), Numerical modeling of asteroid survivability and possible scenarios for the Morokweng crater-forming impact, *Meteoritics & Planetary Science*, *48*(5), 744–757, doi:10.1111/maps.12098.

Quintana, S. N., D. A. Crawford, and P. H. Schultz (2015), Analysis of Impact Melt and Vapor Production in CTH for Planetary Applications, *Procedia Engineering*, *103*, 499–506, doi:10.1016/j.proeng.2015.04.065.

Ricard, Y., D. Bercovici, and F. Albarède (2017), Thermal evolution of planetesimals during accretion, *Icarus*, *285*, 103–117, doi:10.1016/j.icarus.2016.12.020.

Robinson, K. L., and G. J. Taylor (2014), Heterogeneous distribution of water in the Moon, *Nature Geoscience*, *7*(6), 401–408, doi:10.1038/ngeo2173.

1453 Robinson, K. L., J. J. Barnes, K. Nagashima, A. Thomen, I. A. Franchi, G. R.
1454 Huss, M. Anand, and G. J. Taylor (2016), Water in evolved lunar rocks:
1455 Evidence for multiple reservoirs, *Geochimica et Cosmochimica Acta*, *188*, 244–
1456 260, doi:10.1016/j.gca.2016.05.030.

1457 Saal, A. E., E. H. Hauri, M. L. Cascio, J. A. Van Orman, M. C. Rutherford,
1458 and R. F. Cooper (2008), Volatile content of lunar volcanic glasses and the
1459 presence of water in the Moon's interior, *Nature*, *454*(7201), 192–195, doi:
1460 10.1038/nature07047.

1461 Saal, A. E., E. H. Hauri, J. A. Van Orman, and M. J. Rutherford (2013),
1462 Hydrogen Isotopes in Lunar Volcanic Glasses and Melt Inclusions Reveal a
1463 Carbonaceous Chondrite Heritage, *Science*, *340*(6138), 1317–1320, doi:10.
1464 1126/science.1235142.

1465 Saxena, P., L. Elkins-Tanton, N. Petro, and A. Mandell (2017), A model of
1466 the primordial lunar atmosphere, *Earth and Planetary Science Letters*, *474*,
1467 198–205, doi:10.1016/j.epsl.2017.06.031.

1468 Sekine, T., T. Kimura, T. Kobayashi, and T. Mashimo (2015), Dynamic water
1469 loss of antigorite by impact process, *Icarus*, *250*, 1–6, doi:10.1016/j.icarus.
1470 2014.11.008.

1471 Shearer, C. K. (2006), Thermal and Magmatic Evolution of the Moon, *Reviews*
1472 *in Mineralogy and Geochemistry*, *60*(1), 365–518, doi:10.2138/rmg.2006.60.4.

1473 Shoemaker, E. M. (1962), Interpretation of lunar craters, *Physics and Astron-*
1474 *omy of the Moon*, pp. 283–359.

1475 Smith, J. V., A. T. Anderson, R. C. Newton, E. J. Olsen, A. V. Crewe, M. S.
1476 Isaacson, D. Johnson, and P. J. Wyllie (1970), Petrologic history of the moon

inferred from petrography, mineralogy and petrogenesis of Apollo 11 rocks, *Geochimica et Cosmochimica Acta Supplement*, *1*, 897.

Snyder, G. A., L. A. Taylor, and C. R. Neal (1992), A chemical model for generating the sources of mare basalts: Combined equilibrium and fractional crystallization of the lunar magmasphere, *Geochimica et Cosmochimica Acta*, *56*(10), 3809–3823, doi:10.1016/0016-7037(92)90172-F.

Solomatov, V. (2007), Magma Oceans and Primordial Mantle Differentiation, in *Evolution of the Earth*, vol. 9, edited by G. Schubert, pp. 91–119, Elsevier, Amsterdam, doi:10.1016/B978-044452748-6.00141-3.

Stephant, A., M. Anand, R. Tartèse, X. Zhao, G. Degli-Alessandrini, and I. Franchi (2020), The hydrogen isotopic composition of lunar melt inclusions: An interplay of complex magmatic and secondary processes, *Geochimica et Cosmochimica Acta*, *284*, 196–221, doi:10.1016/j.gca.2020.06.017.

Svetsov, V., and V. Shuvalov (2015), Water delivery to the Moon by asteroidal and cometary impacts, *Planetary and Space Science*, *117*, 444–452, doi:10.1016/j.pss.2015.09.011.

Tartèse, R., and M. Anand (2013), Late delivery of chondritic hydrogen into the lunar mantle: Insights from mare basalts, *Earth and Planetary Science Letters*, *361*, 480–486, doi:10.1016/j.epsl.2012.11.015.

Tartèse, R., M. Anand, J. J. Barnes, N. A. Starkey, I. A. Franchi, and Y. Sano (2013), The abundance, distribution, and isotopic composition of Hydrogen in the Moon as revealed by basaltic lunar samples: Implications for the volatile inventory of the Moon, *Geochimica et Cosmochimica Acta*, *122*, 58–74, doi:10.1016/j.gca.2013.08.014.

Thompson, M. A., M. Telus, L. Schaefer, J. J. Fortney, T. Joshi, and D. Lederman (2021), Composition of Terrestrial Exoplanet Atmospheres from Meteorite Outgassing Experiments, *Nature Astronomy*, *5*(6), 575–585, doi:10.1038/s41550-021-01338-8, arXiv: 2104.08360.

Thompson, S. L. (1990), ANEOS analytic equations of state for shock physics codes input manual, *Tech. Rep. SAND-89-2951, 6939284*, Sandia National Labs., Albuquerque, NM (USA), doi:10.2172/6939284.

Trowbridge, A. J., B. C. Johnson, A. M. Freed, and H. J. Melosh (2020), Why the lunar South Pole-Aitken Basin is not a mascon, *Icarus*, *352*, 113,995, doi:10.1016/j.icarus.2020.113995.

Wakita, S., and H. Genda (2019), Fates of hydrous materials during planetesimal collisions, *Icarus*, *328*, 58–68, doi:10.1016/j.icarus.2019.03.008.

Wakita, S., H. Genda, K. Kurosawa, and T. M. Davison (2019), Enhancement of Impact Heating in Pressure-Strengthened Rocks in Oblique Impacts, *Geophysical Research Letters*, *46*(23), 13,678–13,686, doi:10.1029/2019GL085174, _eprint: https://onlinelibrary.wiley.com/doi/pdf/10.1029/2019GL085174.

Wakita, S., H. Genda, K. Kurosawa, T. M. Davison, and B. C. Johnson (2022), Effect of Impact Velocity and Angle on Deformational Heating and Postimpact Temperature, *Journal of Geophysical Research: Planets*, *127*(8), e2022JE007,266, doi:10.1029/2022JE007266.

Warren, P. H. (1985), The Magma Ocean Concept and Lunar Evolution, *Annual Review of Earth and Planetary Sciences*, *13*, 201–240, doi:10.1146/annurev.ea.13.050185.001221.

Wieczorek, M. A. (2009), The Interior Structure of the Moon: What Does Geophysics Have to Say?, *Elements*, *5*(1), 35–40.

Wieczorek, M. A., G. A. Neumann, F. Nimmo, W. S. Kiefer, G. J. Taylor, H. J. Melosh, R. J. Phillips, S. C. Solomon, J. C. Andrews-Hanna, S. W. Asmar, A. S. Konopliv, F. G. Lemoine, D. E. Smith, M. M. Watkins, J. G. Williams, and M. T. Zuber (2013), The Crust of the Moon as Seen by GRAIL, *Science*, *339*(6120), 671–675, doi:10.1126/science.1231530.

Wiggins, S. E., B. C. Johnson, T. J. Bowling, H. J. Melosh, and E. A. Silber (2019), Impact Fragmentation and the Development of the Deep Lunar Megaregolith, *Journal of Geophysical Research: Planets*, *124*(4), 941–957, doi:10.1029/2018JE005757.

Wiggins, S. E., B. C. Johnson, T. J. Bowling, H. J. Melosh, and E. A. Silber (2019), Impact Fragmentation and the Development of the Deep Lunar Megaregolith, *Journal of Geophysical Research (Planets)*, *124*(4), 941–957, doi:10.1029/2018JE005757.

Woo, J., R. Brasser, S. Grimm, M. Timpe, and J. Stadel (2022), The terrestrial planet formation paradox inferred from high-resolution N-body simulations, *Icarus*, *371*, 114,692, doi:10.1016/j.icarus.2021.114692.

Wood, J. A., J. S. Dickey, Jr., U. B. Marvin, and B. N. Powell (1970), Lunar anorthosites and a geophysical model of the moon, *Geochimica et Cosmochimica Acta Supplement*, *1*, 965.

Wünnemann, K., G. Collins, and H. Melosh (2006), A strain-based porosity model for use in hydrocode simulations of impacts and implications for transient crater growth in porous targets, *Icarus*, *180*(2), 514–527, doi:10.1016/j.icarus.2005.10.013.

Zhang, N., M. Ding, M.-H. Zhu, H. Li, H. Li, and Z. Yue (2022), Lunar compositional asymmetry explained by mantle overturn following the

South Pole–Aitken impact, *Nature Geoscience*, *15*(1), 37–41, doi:10.1038/s41561-021-00872-4, publisher: Nature Publishing Group.

Zhu, M.-H., K. Wünnemann, and N. Artemieva (2017), Effects of Moon's Thermal State on the Impact Basin Ejecta Distribution, *Geophys. Res. Lett.*, *44*(22), 11,292–11,300, doi:10.1002/2017GL075405.

Zhu, M.-H., N. Artemieva, A. Morbidelli, Q.-Z. Yin, H. Becker, and K. Wünnemann (2019a), Reconstructing the late-accretion history of the Moon, *Nature*, *571*(7764), 226–229, doi:10.1038/s41586-019-1359-0.

Zhu, M.-H., K. Wünnemann, R. W. Potter, T. Kleine, and A. Morbidelli (2019b), Are the Moon's Nearside-Farside Asymmetries the Result of a Giant Impact?, *Journal of Geophysical Research: Planets*, *124*(8), 2117–2140, doi:10.1029/2018JE005826, _eprint: https://agupubs.onlinelibrary.wiley.com/doi/pdf/10.1029/2018JE005826.

Zhu, M.-H., A. Morbidelli, W. Neumann, Q.-Z. Yin, J. M. D. Day, D. C. Rubie, G. J. Archer, N. Artemieva, H. Becker, and K. Wünnemann (2021), Common feedstocks of late accretion for the terrestrial planets, *Nature Astronomy*, *5*, 1286–1296, doi:10.1038/s41550-021-01475-0.

Table 1: Parameter values for solid layers

Description	Impactor / Mantle	Crust	References
Equation of State	ANEOS dunite	ANEOS granite	
Initial density	3,315 kg m^{-3}	2,630 kg m^{-3}	
Poisson ratio	0.25	0.30	*Ivanov et al.* (2010)
Strength model (ROCK)			
Frictional coefficient (damaged)	0.6	0.8	*Ivanov et al.* (2010)
Frictional coefficient (undamaged)	1.5	1.1	*Ivanov et al.* (2010)
Strength at infinite pressure (damage)	3.5 GPa	2 GPa	*Ivanov et al.* (2010)
Strength at infinite pressure (undamaged)	3.5 GPa	2.5 GPa	*Ivanov et al.* (2010)
Cohesion (damaged)	0.01 MPa	0.01 MPa	*Ivanov et al.* (2010)
Cohesion (undamaged)	50 MPa	10 Mpa	*Ivanov et al.* (2010)
Damage model (Ivanov)			
Ivanov parameter A	10^{-4}	10^{-4}	*Ivanov et al.* (1997)
Ivanov parameter B	10^{-11}	10^{-11}	*Ivanov et al.* (1997)
Ivanov parameter C	$3{\times}10^{8}$	$3{\times}10^{8}$	*Ivanov et al.* (1997)

Table 2: Physical parameter values for numerical models

Planet radius	R	1,740 km
Magma ocean depth	z_{LMO}	300 km
Surface gravity field	g	1.561 m s^{-2}
Escape velocity	v_{esc}	2.33 km s^{-1}
Impactor radius	R_{imp}	25 - 200 km
Impactor velocity	v_{imp}	$1v_{esc}$ - $4v_{esc}$
Crust thickness	δ_{crust}	10 - 80 km
Surface temperature		293 K
Gradient		0.122-0.0161 K m^{-1}
Mantle property (Dunite)		
Initial density	ρ_m	3,315 kg m^{-3}
Crust property (Granite)		
Initial density	ρ_c	2,630 kg m^{-3}
Magma ocean (Dunite)		
Initial density	ρ_{oc}	3,315 kg m^{-3}

Table 3: Resolution parameters for iSALE hydrocode

Domain size	
Horizontal size	2,000 km
Vertical size	10,000 km
Grid spacing	4 km
Cells per projectile radius (CPPR)	
Impactor	25 to 200
Target crust	3 - 25
Target magma ocean	72 - 50
Target mantle	350
Maximum time step (dt_{max})	0.05 s